LIQUEFIED NATURAL GAS (LNG) VAPOR DISPERSION MODELING WITH COMPUTATIONAL FLUID DYNAMICS CODES

A Dissertation

by

RUIFENG QI

Submitted to the Office of Graduate Studies of
Texas A&M University
in partial fulfillment of the requirements for the degree of

DOCTOR OF PHILOSOPHY

August 2011

Major Subject: Chemical Engineering

Liquefied Natural Gas (LNG) Vapor Dispersion Modeling with Computational Fluid Dynamics Codes

LIQUEFIED NATURAL GAS (LNG) VAPOR DISPERSION MODELING WITH COMPUTATIONAL FLUID DYNAMICS CODES

A Dissertation

by

RUIFENG QI

Submitted to the Office of Graduate Studies of
Texas A&M University
in partial fulfillment of the requirements for the degree of

DOCTOR OF PHILOSOPHY

Approved by:

Chair of Committee,	M. Sam Mannan
Committee Members,	Mahmoud El-Halwagi
	Charles Glover
	Yassin A. Hassan
Head of Department,	Michael Pishko

August 2011

Major Subject: Chemical Engineering

ABSTRACT

Liquefied Natural Gas (LNG) Vapor Dispersion Modeling with Computational Fluid Dynamics Codes. (August 2011)

Ruifeng Qi, B.E., Dalian University of Technology, China

Chair of Advisory Committee: Dr. M. Sam Mannan

Federal regulation 49 CFR 193 and standard NFPA 59A require the use of validated consequence models to determine the vapor cloud dispersion exclusion zones for accidental liquefied natural gas (LNG) releases. For modeling purposes, the physical process of dispersion of LNG release can be simply divided into two stages: source term and atmospheric dispersion. The former stage occurs immediately following the release where the behavior of fluids (LNG and its vapor) is mainly controlled by release conditions. After this initial stage, the atmosphere would increasingly dominate the vapor dispersion behavior until it completely dissipates. In this work, these two stages are modeled separately by a source term model and a dispersion model due to the different parameters used to describe the physical process at each stage.

The principal focus of the source term study was on LNG underwater release, since there has been far less research conducted in developing and testing models for the source of LNG release underwater compared to that for LNG release onto land or water. An underwater LNG release test was carried out to understand the phenomena that occur when LNG is released underwater and to determine the characteristics of pool formation

and the vapor cloud generated by the vaporization of LNG underwater. A mathematical model was used and validated against test data to calculate the temperature of the vapor emanating from the water surface.

This work used the ANSYS CFX, a general-purpose computational fluid dynamics (CFD) package, to model LNG vapor dispersion in the atmosphere. The main advantages of CFD codes are that they have the capability of defining flow physics and allowing for the representation of complex geometry and its effects on vapor dispersion. Discussed are important parameters that are essential inputs to the ANSYS CFX simulations, including the mesh size and shape, atmospheric conditions, turbulence from the source term, ground surface roughness height, and effects of obstacles. A sensitivity analysis was conducted to illustrate the impact of key parameters on the accuracy of simulation results.

In addition, a series of medium-scale LNG spill tests have been performed at the Brayton Fire Training Field (BFTF), College Station, TX. The objectives of these tests were to study key parameters of modeling the physical process of LNG vapor dispersion and collect data for validating the ANSYS CFX prediction results. A comparison of test data with simulation results demonstrated that CFX described the physical behavior of LNG vapor dispersion well, and its prediction results of distances to the half lower flammable limit were in good agreement with the test data.

DEDICATION

This dissertation is dedicated to my beloved family and friends.

ACKNOWLEDGEMENTS

I greatly appreciate my advisor and committee chair, Dr. M. Sam Mannan, for his thoughtful guidance and continuous support throughout the course of this research work. His enthusiasm and dedication to process safety development inspires me to pursue process safety engineering and management as my lifetime career. I also would like extend my sincere gratitude to my committee members, Dr. Mahmoud El-Halwagi, Dr. Charles Glover, and Dr. Yassin A. Hassan, for their attention and constructive suggestions. I especially appreciate Dr. Phani Raj for his instruction and contribution to the LNG underwater release study.

Thanks also go to my friends and colleagues from the Mary Kay O'Connor Process Safety Center (MKOPSC) for their encouragement and friendship during my graduate study, especially those in the LNG project – Valerie Green, Dr. Dedy Ng, Dr. Morshed Rana, Dr. Geun Woong Yun, Dr. Benjamin Cormier, Dr. Jaffee Suardin, Carolina Herrera, Byung Kyu Kim. Without their help and support, the completion of this work would not have been possible.

I would like to thank BP Global Gas SPU for financially sponsoring this research work and Texas Engineering Extension Service (TEEX) for providing service during the LNG field tests at Brayton Fire Training Field. Finally, I am grateful to everyone around me for making this period in my life fulfilled and blissful.

NOMENCLATURE

BFTF	Brayton Fire Training Field
CFD	Computational Fluid Dynamics
LFL	Lower Flammable Limit
LNG	Liquefied Natural Gas
MKOPSC	Mary Kay O'Connor Process Safety Center
TEEX	Texas Engineering Extension Service
UFL	Upper Flammable Limit

TABLE OF CONTENTS

Page

Page

Page

LIST OF FIGURES

Page

Page

Page

Page

LIST OF TABLES

Page

1. INTRODUCTION AND LITERATURE REVIEW

1.1 What Is LNG?

Natural gas has become the fastest growing source of energy in the United States. This growth has been driven by the need for cleaner energy, the relative low price of natural gas, and its abundant supplies. By implementing advanced liquefaction technology, natural gas can be purified and refrigerated into a liquid (LNG), which makes it easier to transport and store in tankers. Many onshore or offshore LNG import terminals have been proposed and are expected to be constructed in the next several years to meet the projected significant increase in LNG importation from overseas as a result of growing demand [1, 2].

LNG is natural gas that is refrigerated to its liquid state at approximately -162 °C (-260 °F) under atmospheric pressure. LNG consists mainly of methane and a small portion of ethane, propane, and other heavier hydrocarbons. It is colorless, odorless, non-toxic, non-corrosive and weighs almost 45% of the weight of water. The liquefaction process reduces the volume of natural gas by approximately 600 times, which makes it easier and economically feasible to store and transport by vessels [3].

Table 1 provides the properties and flammable limits of LNG [4].

This dissertation follows the style of Journal of Hazardous Materials.

Table 1. LNG properties and flammable limits

Molecular Weight	μ	16.043	kmol/kg
Critical Temperature	T_c	190.6	K
Critical Pressure	P_c	4.64E+06	Pa
Atmospheric boiling temperature	T_b	111.6	K
Freezing Temperature	T_F	91.0	K
Liquid Density at boiling point (for pure methane)	ρ_L	422.6	kg/m^3
Liquid Density at boiling point (Commercial LNG)	ρ_L	450.0	kg/m^3
Vapor density at boiling point	ρ_v	1.82	kg/m^3
Density of gas at NTP (1 atm, 20 ^oC)	$\rho_{v,\ NTP}$	0.651	kg/m^3
Heat of Vaporization	λ	510	kJ/kg
Heat of Combustion (lower) – LHC	ΔHc	50.0	MJ/kg
Heat of Combustion (higher) – HHC	ΔHc	55.5	MJ/kg
Specific heat of Vapor at constant pressure	C_p	2200	J/kg K
Ratio of specific heats	γ	1.30815	
Stoichiometric Air-fuel mass ratio	r	17.17	
Stoichiometric methane vapor concentration in air		9.5	%
Upper flammability limit in air	UFL	15	%
Lower flammability limit in air	LFL	5	%

1.2 LNG Industry

1.2.1 Demand for LNG

The demand for LNG in the US began in the late 1970s as part of the effort to diversify energy sources in response to the oil crisis. Nowadays the natural gas consumption makes up to 24% of the overall energy consumption in the US, 1.2% of that is imported in the form of LNG. Residential use accounts for 20.9% of total consumption, along with commercial use for 13.4%, industrial use for 28.6%, electrical power for 28.6%, vehicle fuel and other use for 8.5% [5]. According to the projection of Energy Information Administration (EIA), the domestic production of natural gas will increase to 23.5 Tcf by 2035, whereas its consumption will increase to 25 Tcf as shown in Fig. 1 [6]. Thus, imported LNG is considered one of the feasible means to close the gap between production and consumption.

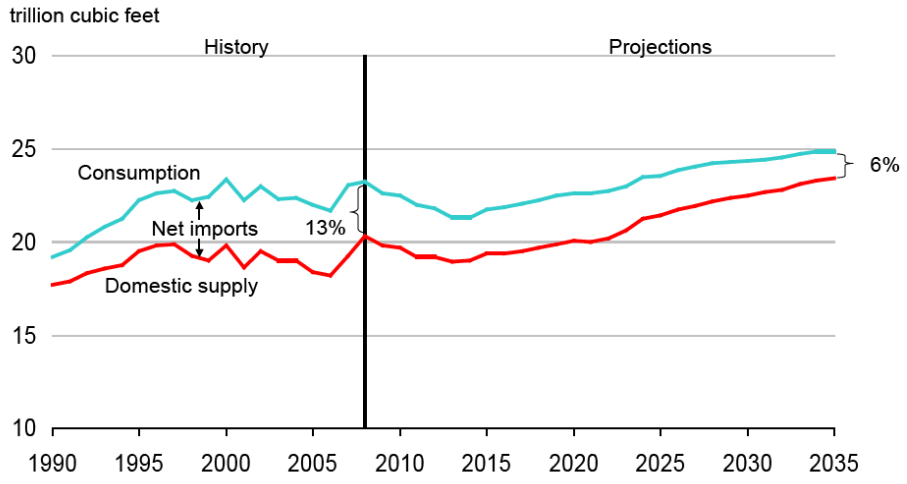

Fig. 1. U.S. natural gas production, consumption and net imports, 1990-2035 (Source: CLNG)

1.2.2 LNG Industry Development in the United States

The LNG industry has a long history in the United States. The first prototype LNG plant commenced construction in West Virginia in 1912 and was put into operation in 1917. The first commercial liquefaction facility was built in Cleveland, Ohio in 1941, which stored LNG in tanks at atmospheric pressure. The first transportation of a large bulk of LNG across the ocean occurred in 1959, in which LNG was carried by an ocean-going vessel (known as The Methane Pioneer) from Lake Charles, Louisiana to Canvey Island, United Kingdom. Between 1971 and 1980, four marine terminals were built in the United States at Lake Charles, Louisiana; Elba Island, Georgia; Cove Point, Maryland; and Everett, Massachusetts allowing for LNG imports from overseas. The first offshore terminal (known as Gulf Gateway Energy Bridge) began operation in 2005 in the Gulf of Mexico, where LNG was regasified offshore on board and was delivered into the onshore grid through a subsea pipeline in the form of high pressure natural gas. Since 2005 another four marine terminals were brought into service, which are located at Freeport, Texas; Sabine, Louisiana; offshore Boston, Massachusetts; and Hackberry, Louisiana. In addition, there are more than 100 peak-shaving facilities storing LNG for the peak demand periods across the United States [3, 7]. Fig. 2 shows the locations of LNG peak-shaving facilities and import terminals by the end of 2008. (The terminal at Hackberry does not appear in this figure since it set operations in July, 2009.)

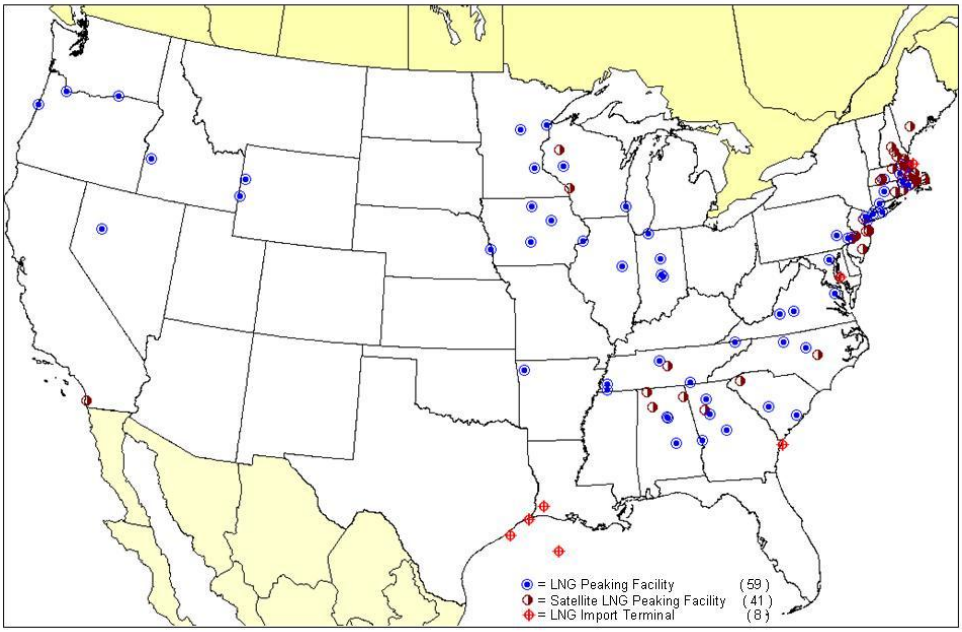

Note: Satellite LNG facilities have no liquefaction facilities. All supplies are transported to the site via tanker truck.
Source: Energy Information Administration, Office of Oil & Gas, Natural Gas Division Gas, Gas Transportation Information System, December 2008.

Fig. 2. U.S. LNG peaking shaving and import terminals, 2008 (Source: EIA)

1.2.3 LNG Supply Chain

The LNG supply chain consists of four interlinked and independently-operated parts: exploration and production, liquefaction, shipping, as well as regasification, storage and distribution.

1.2.3.1 Exploration and Production

The first part of the LNG supply chain is exploration and production. Natural gas is a fossil fuel which deposits under the land and sea. The U.S. and North America have ample natural gas resources. The proved natural gas reserves in the U.S. have increased from 167.4 Tcf to 244.7 Tcf from 1999 to 2009 [8]. Exploration activities involve

seismic measurements, drilling and well completions. Once the well is successfully completed, the natural gas is produced from reservoirs and then is transported from the wellhead to a processing facility via high pressure pipelines. The composition of natural gas varies depending on where the gas reservoir is [9].

1.2.3.2 Liquefaction

Liquefaction is another key part of the LNG supply chain. The major process in an LNG liquefaction plant is shown in Fig. 3 [10]. Liquefaction plants often consist of several parallel units or "trains".

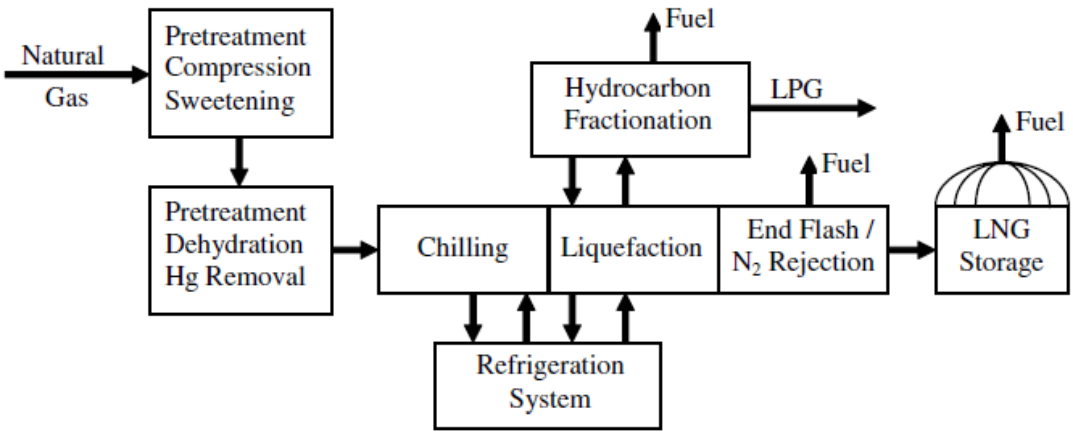

Fig. 3. Typical LNG liquefaction plant process flow diagram [10]

The natural gas first passes through pretreatment to remove contaminants or impurities including non-hydrocarbon gases and water. Heavier hydrocarbons are then removed using high level refrigerant to prevent freezing and equipment damage when the gas is cooled to approximately -256 °F and to meet quality specifications at the

delivery point. The residue gas mainly composed of methane is further cooled until completely liquefied. During the liquefaction, the volume of gas is reduced by a factor of 600, which makes LNG only uses 1/600th of the space required for a comparable amount of natural gas at room temperature and atmospheric pressure.

The LNG is stored in double-walled tanks at atmospheric pressure. The inner wall is in contact with the LNG and is made of materials suitable for cryogenic service. These materials include 9 % nickel steel, aluminum or other cryogenic alloy. The outer wall is generally made of carbon steel or reinforced concrete. The annular space between two tank walls is filled with insulation material [7, 9].

1.2.3.3 Shipping

LNG tankers are specially designed ships to transport LNG across the seas. These tankers are constructed with double hulls to increase the integrity of the containment system and prevent leakage or rupture in an accident. Three types of cargo containment systems have evolved as industry standards. They are: 1) the spherical (Moss) design shown in Fig. 4 [9]; 2) the membrane design shown in Fig. 5 [9]; and 3) the structural prismatic design. Many LNG tankers currently in service use Moss design, which are easily identifiable because of the visible top half of the spherical tanks above deck. The capacity of an LNG vessel grew considerably from less than 30,000 m^3 in the mid 1960s to over 250,000 m^3 in 2009. Compared with other shipping vessels, LNG vessels are generally less polluting because they burn natural gas instead of fuel oil for propulsion [7, 9].

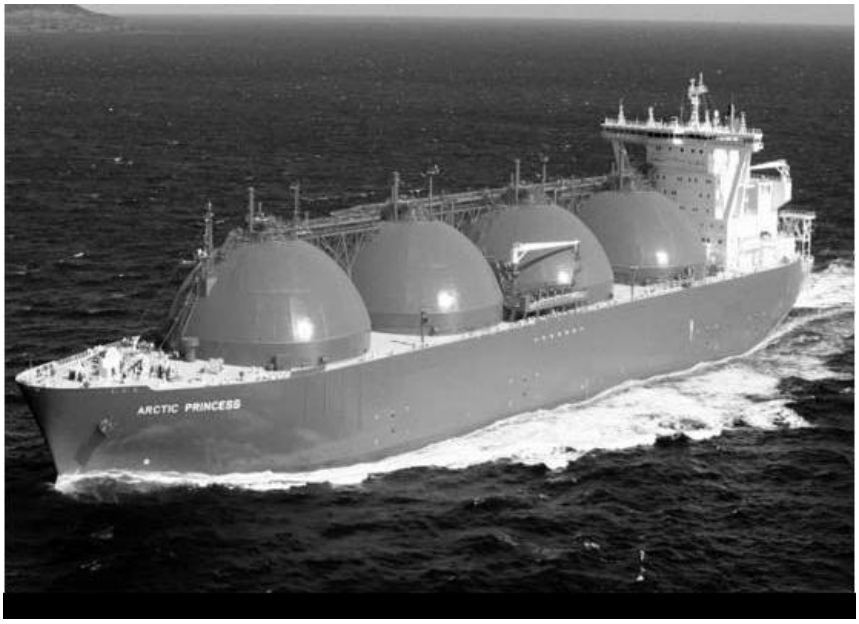

Fig. 4. Moss type LNG tanker [9]

Fig. 5. Membrane type LNG tanker [9]

1.2.3.4 Storage and Regasification

LNG is used in various ways upon arrival at its destination. LNG receiving terminals may include facilities to directly load LNG into tanker trucks for road distribution. Or, LNG import terminals may be located with power stations, allowing the use of such cryogenic liquid to help cool the power plant where natural gas is burned for electricity generation. In most cases, LNG is first transferred to double-walled storage tanks, similar to those used in the liquefaction plant where LNG is stored at atmospheric pressure until needed. Then LNG is pumped at higher pressure through regasification process where it is converted back to its gaseous state. The LNG is warmed in a controlled environment by passing through either pipes heated by direct-fired heaters, or pipes warmed by seawater or hot water. The revaporized natural gas is then regulated for pressure and is transported to residential and commercial customers via pipeline system [7, 9].

1.2.4 Significant Accidents in LNG Industry

Two most quoted accidents related to LNG facilities and transportation are presented below since they both had a significant impact on public perception, industry standards and safety practice of LNG operations.

1.2.4.1 Cleveland, Ohio, 1944

In 1941, the East Ohio Gas Company built a commercial LNG peak-shaving facility in Cleveland, Ohio. The facility was operated without incident until a larger new

tank was added in 1944. A shortage of stainless steel alloys during World War II led to compromises in the design of the new tank. The tank failed shortly after it was placed in service. LNG spilled out, forming a flammable vapor cloud that filled the surrounding streets and storm sewer system. The cloud was promptly ignited resulting in 128 fatalities and 225 injuries in the adjoining residential area. The conclusion of the investigating body, the U.S. Bureau of Mines, was that the concept of liquefying and storing LNG was valid if "proper precautions were observed." In fact, LNG tanks properly constructed of nine percent nickel steel have never had a crack failure in the 35-year history since the Cleveland incident [11].

1.2.4.2 Cove Point, Maryland, 1979

In October 1979, an explosion occurred within an electrical substation at the Cove Point, MD receiving terminal. LNG leaked through an inadequately tightened LNG pump electrical penetration seal, vaporized, passed through 200 feet of underground electrical conduit, and entered the substation. Since natural gas was never expected in this building, there were no gas detectors installed in the building. The natural gas-air mixture was ignited by the normal arcing contacts of a circuit breaker resulting in an explosion. The explosion killed one operator in the building, seriously injured a second and caused about $3 million in damages [12].

This was an isolated accident caused by a very specific set of circumstances. The National Transportation Safety Board found that the Cove Point Terminal was designed and constructed in conformance with all appropriate regulations and codes. However, as

a result of this accident, three major design code changes were made at the Cove Point facility prior to reopening. Those changes are applicable industry-wide [12].

1.2.5 Regulatory Authorities and Regulations

1.2.5.1 Jurisdiction Authorities

The Federal Energy Regulatory Commission (FERC) is authorized under the Natural Gas Act to approve the siting of onshore LNG terminals. The U.S. Coast Guard (USCG), along with the Department of Transportation Maritime Administration has jurisdiction under the Deep Water Port Act to approve the siting of offshore LNG facilities. The U.S. Environmental Protection Agency and state environmental agencies establish air and water standards with which the LNG industry must comply. Other federal agencies involved in environmental protection and safety protection include the U.S. Fish and Wildlife Service, U.S. Army Corps of Engineers (for coastal facilities and wetlands), U.S. Minerals Management Service (for offshore activities) and National Oceanic and Atmospheric Administration (for any activities near marine sanctuaries). The U.S. Department of Energy - Office of Fossil Energy helps to coordinate across federal agencies that have regulatory and policy authority for LNG. State, county and local (municipal) agencies play roles to ensure safe and environmentally sound construction and operation of LNG industry facilities. The LNG industry is responsible for safe operations and facility security in cooperation with local police and fire departments [13].

1.2.5.2 Codes, Standards and Regulations

Major codes and standards regulations applicable to LNG operations are summarized as follows [14]:

- 49 CFR Part 193, Liquefied Natural Gas Facilities: Federal Safety Standards
- 33 CFR Part 127, Waterfront Facilities Handling Liquefied Natural Gas and Liquefied Hazardous Gas
- NFPA 59A, Standard for the Production, Storage, and Handling of Liquefied Natural Gas (LNG)
- NFPA 57, Standard for Liquefied Natural Gas (LNG) Vehicular Fuel Systems
- EN 1473, Installation and Equipment for Liquefied Natural Gas—Design of Onshore Installations
- EN 1160, Installations and Equipment for Liquefied Natural Gas - General Characteristics of Liquefied Natural Gas
- EN 14620, Design and Manufacture of Site Built, Vertical, Cylindrical, Flat-bottomed Steel Tanks for the storage of refrigerated, liquefied gases with operating temperatures between 0 °C and -165 °C

It is noted that no requirements or standards are applicable to LNG spills onto water.

1.3 LNG Hazards

The LNG industry keeps an excellent safety record over the last thirty years. In order to maintain this record, hazards related to handling of LNG should be addressed

and fully understood in design, construction, and operations of every part of LNG supply chain. The major hazards posed by an accidental LNG spill are described in the following paragraphs.

1.3.1 Cryogenic Hazards

LNG is cryogenic liquid. When it comes into contact with the skin or other living tissues, it vaporizes rapidly and causes 'cold burn' or frostbite. The vapor from LNG remains very cold and is therefore heavier than air. If large amount of vapor accumulates near the ground, it displaces ambient air. Exposure of people to such a lean oxygen environment could lead to asphyxiation and even death. Many materials such as rubber, plastic and carbon steel can become brittle at extremely cold temperature so that they lose their resilience to withstand impact stress and are susceptible to fail. It is important to keep in mind that any material subject to cold embrittlement must be avoided when selecting proper material for equipment involved in LNG operations [14-17].

1.3.2 Pressure Buildup

LNG has a high expansion ratio (~600:1) between its gaseous state and liquid state. Without sufficient venting or pressure relief devices, heated LNG will generate a large amount of vapor and cause rapid pressure build up in a container [14-17].

1.3.3 Flammable Vapor Cloud/Flash Fire

LNG will evaporate upon release and the vapor generated by this boiling liquid will start to mix with the surrounding air and will be carried downwind with the air creating a heavier-than-air, cold vapor. As the cold vapor cloud continues to be carried downwind, it will mix with additional air and be further diluted. However, some portion of the vapor cloud will be within the flammable limits (between 4.4-16.5% volumetric concentration mixture with air). If this flammable portion comes in contact with an ignition source, the vapor cloud may ignite. The flame might then propagate through the cloud, back to the source of the vapor, particularly if the flammable portion of the cloud is continuous. This simple burn-back of an unconfined vapor cloud can cause secondary fires by igniting materials in the path of the flame and can cause severe burns to persons caught within the cloud. Damage to equipment will generally be limited since the time of exposure to the fire will be relatively short [14-17].

1.3.4 Rollover

The addition of LNG with different densities to partially filled LNG tanks or preferable evaporation has been known to lead to the formation of stratified layers. The density difference may be due to different sources of LNG or the weathering of LNG in the tank. Due to heat and mass transfer, the densities of the two layers approach each other. Eventually, these two layers mix resulting in a sudden increase in the vapor evolution and sometimes tank pressure. Rollover may result in the excessive loss of valuable fuel at best, or lead to an incident under extreme conditions [14-17].

1.3.5 Rapid Phase Transition

The phenomenon of rapid vapor formation with loud "bangs" has been observed when LNG is released under water. This non-flaming physical interaction is referred to as "rapid phase transition" or "flameless explosion" [14-17].

1.4 LNG Spills Experiments

1.4.1 Burro Series

The Burro tests were performed by the Lawrence Livermore National Laboratory (LLNL) at the Naval Weapons Center at China Lake, California and sponsored by the U.S. DOE and the Gas Research Institute. A total of 8 LNG releases onto water were performed with spill volumes ranging from 24 to 39 m^3 (848–1377 ft^3), spill rates of 11.3–18.4 m^3/min (399–650 ft^3/min), wind speeds from 1.8 to 9.1 m/s (4–20 mph), and atmospheric stability conditions from unstable to slightly stable. Dispersion occurred over water for 29 m (95 ft) from the spill point on a 58 m (190 ft) diameter pond, 1m (3.3 ft) deep, then over land for 80 m (262 ft) where the terrain was irregular with a rise of 7 m (23 ft). Beyond this point, the land was relatively level [18, 19].

Measurements of wind speed and direction, gas concentration, temperature, humidity, and heat flux from the ground were made at several distances from the spill and at several elevations. Gas concentration measurements were averaged over 10 s durations. High-frequency data indicated that significant fluctuations about the 10 s average occurred such that the instantaneous flammable extent of the gas cloud will be larger than is indicated by the mean LFL contour. Differential boil-off was observed in

the tests where ethane and propane enrichment up to 40% in the cloud occurred late in the spills and propagated downwind up to 140 m (459 ft). It was also found that a relative increase in absolute humidity is correlated to an increase in gas concentration. A 1% gas concentration in the cloud was associated with a 15% increase in absolute humidity. Thus, water was entrained into the cloud such that the water content of the gas cloud was substantially higher than the ambient air [18, 19].

1.4.2 Maplin Sands

In 1980, tests were conducted at Maplin Sands, England by the National Maritime Institute and were sponsored by Shell. The main purpose of these tests was to obtain data for dispersion and radiation due to fire. Twenty-four continuous and ten instantaneous spills were performed at average wind speeds of 3.8–8.1 m/s (8.5–18 mph). Instantaneous spills were performed by rapidly sinking a barge loaded with LNG or propane. For the instantaneous spills, the spill volumes tested were 5–20 m^3 (178–710 ft^3), and for continuous spills, spill rates were 1.5–4 m^3/min (53–141 ft^3/min). A 300 m (984 ft) diameter dike surrounded the spill point for containment. It was found that the dispersion behavior of the cloud was affected by the method of LNG release. For an underwater release, a more buoyant cloud resulted, whereas with an above-water release, a lower and longer downwind cloud resulted. An RPT was observed in one of the instantaneous LNG spills, resulting in a maximum overpressure of 1.8 kPa (0.26 psi) and damage to the barge.

A typical pool radius was roughly 10 m (33 ft), and the evaporation rate was calculated to be approximately 2×10^{-4} m/s (6.6×10^{-4} ft/s). Pool radius as a function of spill rate was not reported. Using a 3-s average measurement, the maximum dispersion distance to LFL for a spill rate of 3.2 m^3/min (114 ft^3/min) and wind speed of 5.5 m/s (12 mph) was 190 ± 20 m (623 ± 66 ft) downwind of the spill. The distance to LFL was found to be within the visible boundary of the vapor cloud for a calculated humidity range of 50–100% [20].

1.4.3 Coyote Series

The Coyote tests were performed by LLNL and the Naval Weapons Center at China Lake, California and sponsored by the U.S. DOE and the Gas Research Institute. The burning of vapor clouds from LNG spills on water were studied in order to determine fire spread, flame propagation, and heat flux. Data on 4 spills of 14.6–28 m^3 (516–989 ft^3) with flow rates of 13.5–17.1 m3/min (44.3–56.1 ft^3/min) were performed with fuel of varying ratios of methane, propane, and ethane. Tests were performed in wind speeds from 4.6 to 9.7 m/s (10–22 mph) and atmospheric stability conditions from unstable to neutral. Gas concentration measurements were averaged over a 2 s period.

In the test with the highest flow rate or total volume spilled, 17.1 m^3/min or 28 m^3 (604 ft^3/min or 989 ft^3), RPTs increased the distance to the downwind LFL by about 65% and the total burn area by about 200%. The authors note that the increase was caused by an increased source rate and by enrichment in higher hydrocarbons. The puffs of vapor from the RPTs cause momentary increases in concentration as they propagate

downwind. The test conducted in the lowest wind speed and most stable atmospheric conditions had the broadest vapor fire cloud with a maximum width of 130 m (426 ft) and downwind distance of 210 m (689 ft) [21].

1.4.4 Falcon Series

The Falcon tests were conducted at Frenchman Flat in Nevada by LLNL and sponsored by the Gas Research Institute and the U.S. DOT. The objectives of the tests were to provide a database on LNG vapor dispersion from spills involving obstacles and to assess the effectiveness of vapor fences for mitigating dispersion hazards. The testing was performed on a 40 m × 60 m (131 × 197 ft) pond enclosed by an 88m (289 ft) long by 44 m (144 ft) wide by 9.1 m (30 ft) high vapor fence. A 22 m (72 ft) wide by 13.7m (45 ft) high barrier was placed upwind of the pond in order to simulate the obstruction of a storage tank. Five tests were performed with spill rates of 8.7–30.3 m^3/min (107–1070 ft^3/min), volumes of 20.6–66.4 m3 (727–2345 ft^3), wind speeds of 1.7–5.3 m/s (3.8–12 mph), and methane concentrations of 88–94.7%. Gas concentration and temperature measurements were taken at towers upwind and downwind of the spill.

Tests were performed with and without the vapor fence. With the fence, the downwind distance to the 2.5% concentration on the ground was reduced from approximately 380 m to 235 m (1246–771 ft) and a substantial reduction in the hazardous areas was also achieved. The persistence of the cloud at a 2.5% concentration near the center of the spill was 530 s with the fence versus 330 s without the fence. Although the fence reduced the downwind distance of the hazardous area and delayed

cloud arrival time, it prolonged the cloud persistence time within the fence thereby prolonging the potential for ignition given a source within the reduced area [22].

1.5 LNG Hazard Consequence Modeling

1.5.1 Source Term Modeling

When LNG accidentally escapes its containment, a pool is usually considered to form, which provides, by means of spreading and vaporization, a source of a flammable heavy gas cloud. The 'source term' is thus usually considered to be the pool, and a considerable amount of research has been done over the years on liquid pool source terms.

1.5.1.1 Release Rate

A mechanical energy balance associated with fluid flow is used to calculate release rate through a hole in an LNG storage tank [23]:

$$\int \frac{dP}{\rho} + \Delta\left(\frac{\bar{u}^2}{2\alpha g_c}\right) + \frac{g}{g_c}\Delta z + F = -\frac{W_s}{\dot{m}} \tag{1}$$

where

P = the pressure

ρ = the density of the liquid

u = the average instantaneous velocity of the fluid

g_c = the gravitational constant

α = the unitless velocity profile correction factor with the following values: α = 0.5 for laminar flow, α = 1.0 for plug flow, and $\alpha \rightarrow 1.0$ for turbulent flow

g = the acceleration due to gravity

z = the height above datum

F = the net friction loss term

Ws = the shaft work

$\dot{m}$ = the mass flow rate

For incompressible liquid, the density is constant, so

$$\int \frac{dP}{\rho} = \frac{\Delta P}{\rho} \tag{2}$$

Assuming a constant gauge pressure P_{Tank} in the storage tank, then

$$\Delta P = P_{Tank} \tag{3}$$

The shaft work is zero, and velocity of the fluid in the tank is assumed negligible. The frictional losses in the leak can be approximated by a constant discharge coefficient C_1, which is defined as

$$-\frac{\Delta P}{\rho} - F = C_1^2 \left(-\frac{\Delta P}{\rho}\right) = C_1^2 \left(\frac{P_{Tank}}{\rho}\right) \tag{4}$$

A hole develops at a height h_L below the liquid level, namely $\Delta z = h_L$

The average discharge velocity is

$$\bar{u} = C_1 \sqrt{\alpha} \sqrt{2 \left(\frac{g_c P_{Tank}}{\rho} + g h_L\right)} \tag{5}$$

A new discharge coefficient C_d is defined as

$$C_d = C_1\sqrt{\alpha} \tag{6}$$

The mass release rate Q_m from a hole of area A in the LNG tank is given by [23]

$$Q_m = \rho\bar{u}A = \rho A C_0 \sqrt{2\left(\frac{g_c P_{Tank}}{\rho} + g h_L\right)} \tag{7}$$

Q_m = the mass flow rate

ρ = the density of liquid

$\bar{u}$ = the mean liquid velocity

A = the orifice area

C_d = the discharge coefficient

P_{tank} = the gauge pressure inside of the tank

h_L = the level of liquid in the tank

g_c = the gravitational constant

g = the acceleration due to gravity

1.5.1.2 Pool Spreading

Pool area and vaporization rate are essential inputs for any kind of vapor dispersion model. The pool area and shape identify the source scope and depend on the surface properties and geometry of the spill area. In most LNG onshore import terminals, dikes or bunds are built around the storage tanks in order to contain spilled liquids. Therefore, when LNG is released into such an impoundment area, the maximum extent

of the LNG pool is always taken as the same area and shape of the impoundment due to the presence of a boundary.

A spreading pool model was derived by Fay [24], which is applicable to cryogenic liquid pool spreading. The model identifies three consecutive regimes of pool spreading. During each regime, certain forces are dominant while others are negligible. These regimes include:

1. Gravity-Inertia Regime: gravity and inertia forces are dominant
2. Gravity-Viscous Regime: viscous force becomes important
3. Surface Tension-Viscous Regime: the surface tension becomes dominant

A cryogenic liquid spreading on the water surface will evaporate. Most of the evaporation and spreading occurs only in the gravity inertia regime [25]. Therefore, the Gravity-Inertia regime model described below is used to predict the pool spreading. The main driving force is gravity which pushes horizontally on the pool to spread the pool sideways and counterbalances with the inertial resistance of the liquid.

The spreading pool is assumed to be a circular cylinder of radius r and uniform height h, as shown in Fig. 6.

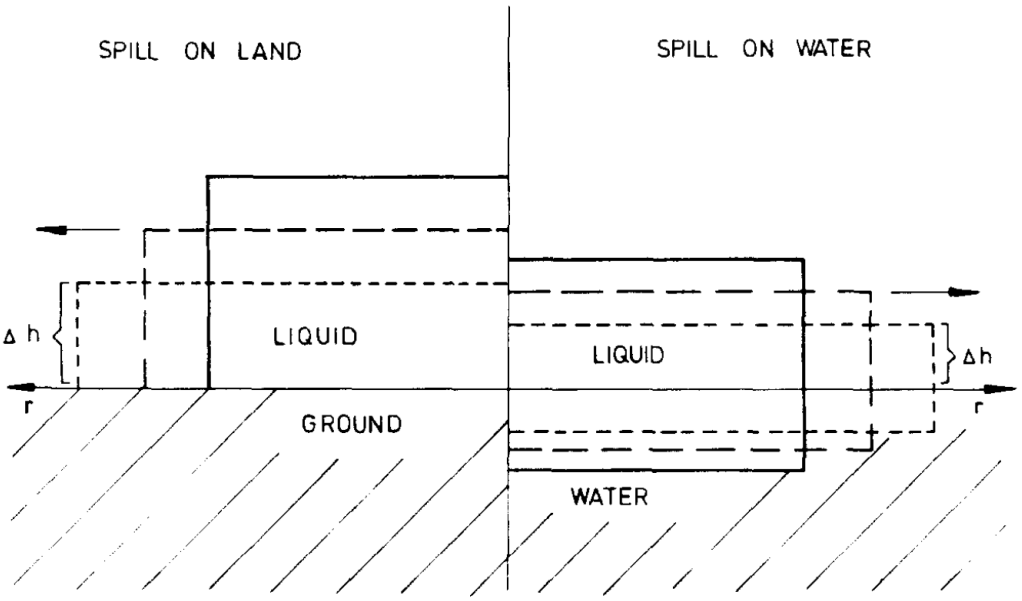

Fig. 6. Model representation of liquid spread on land and water [25]

Then the momentum balance can be written as [25]

$$\rho\pi r^2 hg\frac{\Delta h}{r} = -\frac{1}{\varepsilon}\rho\pi r^2 h\frac{d^2 r}{dt^2} \tag{8}$$

with dr/dt=0 at t=0

Therefore

$$\frac{dr}{dt} = (\varepsilon g\Delta h)^{1/2} \tag{9}$$

where

$\Delta h = h$ for LNG spill on land

$\Delta h = h\left(\frac{\rho_w - \rho}{\rho_w}\right)$ for LNG spill on water

h = the thickness

V = the total volume on spread on water

r = the radius of the pool, assuming that the pool is a circle

g = the acceleration due to gravity

ε = the inertia factor =2

ρ_w = the water density

ρ = the cryogenic liquid density

1.5.1.3 Vaporization Rate

The vaporization rate is calculated based on heat transfer /heat flux from ambient environment to an LNG pool. Fig. 7 shows possible heat transfer around a pool.

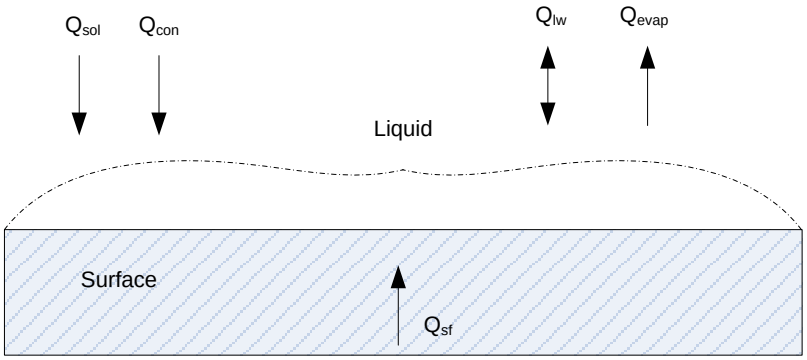

Fig. 7. Heat transfer around an LNG pool [26]

The energy balance may be expressed with the following equation [26]:

$$\frac{dQ_t}{dt} = \frac{dQ_{lw}}{dt} + \frac{dQ_{sol}}{dt} + \frac{dQ_{con}}{dt} + \frac{dQ_{grd}}{dt} - \frac{dQ_{evap}}{dt} \quad (10)$$

where

Q_t = the total energy

Q_{con} = the surface conduction

Q_{sol} = the solar insolation

Q_{lw} = the long wave radiation

Q_{sf} = the convection from surface

Q_{evap} = the heat lost to evaporation

The general formula for the energy balance can be simplified according to the specific scenario. The difference in temperature between the surface and the cryogenic liquid affects the heat conduction modes. With a high temperature difference, film boiling may apply. With a low temperature difference, nucleate boiling may apply.

1.5.2 Vapor Dispersion Modeling

Methane has a low molecular weight (16.04 g/mol) indicating it is lighter than air under normal conditions. However, the density of methane at its boiling point (1.82 kg/m^3) is much higher than that of air at ambient temperature, thus LNG vapor cloud behave like dense gas in the atmosphere in the event of an accidental release. It is flammable in air over a narrow range of concentrations from 5% - 15 % by volume.

A broad range of consequence models have been developed to model LNG vapor dispersion and to determine exclusion zones. These models are usually categorized into four groups: Workbooks /Empirical Correlations, Integral model, Shallow layer model and Computational Fluid Dynamics (CFD) model.

1.5.2.1 Empirical Correlations

The simplest models are modified Gaussian puff/plume models that are based upon the conservation of species equation. The downwind concentration profiles are represented by ad hoc equations. The cloud is assumed to have a specific Gaussian shape with air entrainment occurring at the cloud edges and the interior of the cloud is assumed to have a uniform composition [23].

1.5.2.2 Integral Models

One-dimensional integral models such as SLAB, HEGADAS and DEGADIS use similarity profiles that assume a specific shape for the crosswind profile of concentration and other properties. The downwind variations of spatially averaged, crosswind values are determined by using the conservation equations in the downwind direction only. The weakness of these models is that they cannot model flow around obstacles or over complex terrain [27-29].

1.5.2.3 Shallow-Layer Models

Shallow-layer models use equations that assume the lateral dimensions are much greater than the vertical dimension, which is representative of dense gas releases where low wide clouds result. Depth-averaged variables are solved in two dimensions (lateral) using the conservation equations. Empirical correlations are used to determine the entrainment rate of air into the dense plume. The ability to model the effects of complex terrain and phase changes can be incorporated into this model. It is a compromise

between Navier–Stokes based models and one-dimensional integral models, though it still requires an order of magnitude greater computational time then one-dimensional integral models [30].

1.5.2.4 Computational Fluid Dynamics (CFD)

The most complex models are those that computationally solve time-averaged, three-dimensional turbulent transport equations that come from conservation of mass, species, momentum, and energy balances. These codes are termed CFD models and are based upon solving the Navier–Stokes fluid equations. The most well-known code for dispersion that is of this model type is FEM3 and its subsequent upgraded versions up to FEM3C. Developed by the Lawrence Livermore National Laboratory, FEM3 uses a finite element scheme in space and a finite difference scheme in time. It models flow over variable terrain and objects, as well as complex cloud structures such as vortices and bifurcation. Both isothermal and non-isothermal dense gas releases as well as neutrally buoyant vapor emissions can be modeled. It has the capability to model multiple simultaneous sources of instantaneous, continuous, and finite-duration releases. FEM3C also incorporates a phase change model that accounts for water vapor interaction in the cloud, and it has the option to use the k-epsilon turbulent transport equations [31, 32]. Limitations of these codes are in the approximations and assumptions that are used to model turbulence and buoyancy effects. They are the most computationally expensive among the model types, but with the present day computational power, they can be run on a single processor personal computer.

1.6 Statement of Problem and Significance

Consequence modeling for LNG vapor dispersion plays a vital role in the risk assessment of LNG operations to determine potential hazardous impact of worst credible accidents. One of the major hazards concerned by industry is the flammable vapor cloud drifting with wind direction in the event of an accidental LNG spill. Two major types of models for LNG vapor dispersion are integral models and CFD models. Integral models such as DEGADIS, SLAB, HEGADAS, and many others are widely used because of their fast computational time and ease of use. However, most integral models are not able to take into account geometry effects on vapor cloud and turbulence because of their limitations in describing the terrain and congestion density of obstacles in LNG spill scenarios. Recent advancements in computation capabilities, including processing capacity and memory space, have made it possible for engineers to utilize CFD to solve complex fluid flow problems. CFD models are able to provide a detailed description of physical processes and handle complex geometries, and can thus be used to predict the behavior of LNG vapor cloud dispersion in a site-specific risk analysis. However, CFD simulation setup methods for LNG vapor dispersion and their validation against actual large or medium-scale spill tests have not been sufficiently reported in the literature.

In addition, to obtain sufficient trust in using CFD models as a prediction tool, an extensive study of parameters influencing simulation results is needed to estimate and control the magnitude of uncertainties to a prescribed confidence level.

1.7 Proposed Research

1.7.1 Objectives

The objectives of this research were:

- To improve the understanding of physical process of LNG vapor dispersion under different release conditions.
- To develop a CFD-based modeling tool dedicated to the prediction of vapor dispersion of LNG release, including obstacle and terrain effects.
- To provide guidance on the application of CFD models to address complex LNG dispersion scenarios and to generate reliable prediction results.

1.7.2 Methodology

To achieve the objectives above, a research outline was developed as shown in Fig. 8. For modeling purposes, the physical process of the dispersion of LNG releases is divided into two stages: source term and atmospheric dispersion. These two stages are modeled separately by a source term model and a dispersion model due to the different parameters used to describe the physical behavior at each stage.

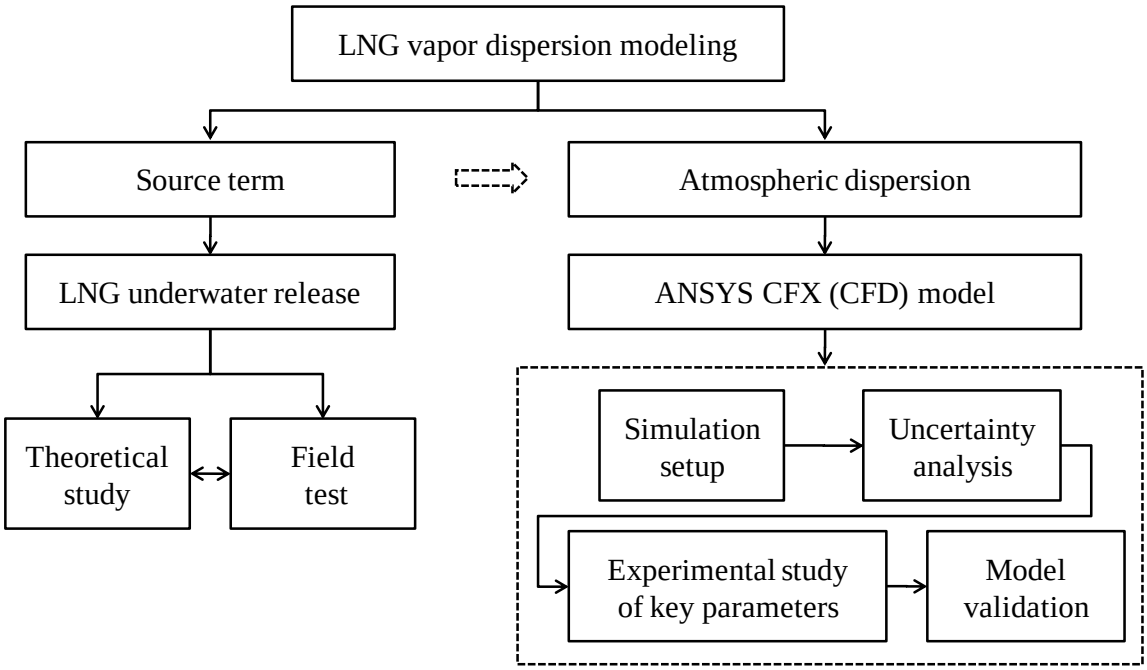

Fig. 8. Research outline

The principal focus of the source term study was on LNG underwater release, since there has been far less research conducted in developing and testing models for the source of LNG release underwater compared to that for LNG release onto land or water. An underwater LNG release test was carried out to understand the phenomena that occur when LNG is released underwater and to determine the characteristics of pool formation and the vapor cloud generated by the vaporization of LNG underwater. A mathematical model was used and validated against test data to calculate the temperature of the vapor emanating from the water surface.

ANSYS CFX, a general-purpose computational fluid dynamics (CFD) package, was employed to model atmospheric LNG vapor dispersion. A modeling setup method was developed and input parameters associated with the domain and boundary

conditions were discussed. A sensitivity analysis was conducted to illustrate the impact of key parameters on the accuracy of simulation results. Moreover, a set of medium-scale LNG spill tests were performed at the BFTF to study the physical process of LNG vapor dispersion under different release conditions. The experimental data collected from those tests were also used to validate ANSYS CFX simulation results.

2. MKOPSC LNG SPILL FIELD EXPERIMENTS

2.1 Background

Since 2005, BP Global Gas SPU and the Mary Kay O'Connor Process Safety Center (MKOPSC) have jointly established a research and development program to investigate LNG spill emergency response and hazard control. A series of medium-scale field tests have been carried out at the Brayton Fire Training Field (BFTF). The focus of the tests was in the following three areas:

1) LNG vapor dispersion: studying key physical parameters for CFD modeling of LNG vapor dispersion and obtaining a relevant database for model validation.
2) Water curtain application: examining the effectiveness of water curtains for mitigation of horizontal dispersion of LNG vapor and studying the major physical mechanisms of gas-liquid interaction in two specific types of water curtain.
3) Application of high expansion foam: studying the effectiveness of foam for vapor control and pool fire mitigation.

2.2 BFTF LNG Test Facilities

BFTF is located in College Station, TX and is affiliated with Texas Engineering Extension Service (TEEX) which is a member of the Texas A&M University system. One of the primary missions of BFTF is to provide education and training for firefighters

and emergency responders so that they can cope with the various hazards they may encounter including those associated with LNG spills. These include cryogenic hazard, flammable vapor cloud dispersion, and pool fire. To this end, LNG props were developed with the sponsorship of BP to create four scenarios for trainees. The props are composed of three concrete pits and one L-shape trench, as illustrated in photograph shown in Fig. 9.

Fig. 9. Brayton Fire Training Field (BFTF) LNG training props

2.3 LNG Vapor Dispersion Experiments

Between 2005 and 2009, six series of small- and medium-scale LNG spill tests were carried out by MKOPSC, together with TEEX, at BFTF. These tests covered a

wide range of release scenarios including LNG vapor dispersion with or without vapor fence, application of water curtain, and application of high expansion foam and foam glass to LNG pool fire. All of these tests were with LNG containing 98%-99.8% methane and were highly instrumented to measure parameters of interest. In each day of testing, approximately 11000 gallons (41 m^3) of LNG was spilled into purpose built concrete pits: in some cases these contained water. A brief description of the LNG vapor dispersion experiments is presented in the following paragraphs. Water curtain and high expansion application experiments together with data analysis are published in other researchers' work in this program [33, 34]. Full details of these tests are provided in MKOPSC LNG test data report [35].

2.3.1 2006 LNG Vapor Dispersion Test

Pit 3 (6.71m × 6.71m ×2.44 m) was used to perform this test, which is shown in Fig. 10. The pit was filled with water to the brim. A foam generator (shown on the right-hand side of Fig. 10) was installed at a 1.22 m elevation near the pit to apply high-expansion foam in case of an emergency. A total of approximately 4 m^3 of LNG was released onto the water via a 76-mm-diameter delivery pipe with a flow rate of about 0.265 m^3/min. The large amount of water below the LNG promoted vaporization and kept the vaporization rate essentially equal to the LNG discharge rate. Two weather stations were installed at elevations of 3 and 10 m to collect local weather data, including the wind direction, wind speed, humidity, temperature, and atmospheric pressure. Two thermocouples and two gas detectors were placed in the center of the pit,

1.22 m above the water. Additionally, 16 gas detectors were installed at different downwind distances and elevations (0.30 m and 1.22 m above the ground) to measure the vapor concentration. All of these gas detectors have an accuracy of ± 2% v/v and their measurement rates are for every second.

Fig. 10. 2006 LNG vapor dispersion test setup

2.3.2 2007 LNG Vapor Dispersion Test

Pit 2 (10.06m × 6.4m × 1.22m) was filled with water to create a water pond for the LNG release test, as shown in Fig. 11. 1.2 m-high wooden boards were erected around the pit as obstacles. LNG was released onto the water via the same delivery pipe with a flow rate of about 0.75 m^3/min. Two foam generators were installed at a 1.22 m elevation above the pit so as to apply high expansion foam in the following pool fire test. An array of instrumentation, which was composed of 2 weather conditions, 40 gas

detectors, 1 cryogenic flow meter and 92 thermocouples, was utilized at the source area and downwind to measure and record the variables of interest. The setup of poles to support gas detectors is shown in Fig. 12 and the positions of gas detectors are listed in Table 2.

Fig. 11. 2007 LNG vapor dispersion test setup

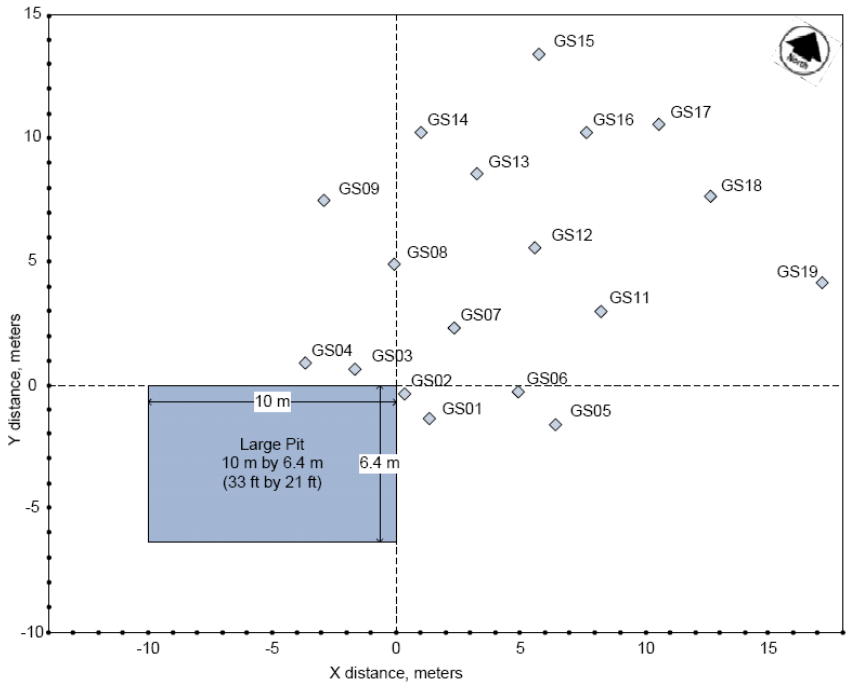

Fig. 12. Gas detector pole locations in 2007 LNG vapor dispersion test

Table 2. Gas detector positions in 2007 LNG vapor dispersion test

Pole No.	Gas detector position				Pole position in Fig. 12	
	Low	Bottom	Middle	Top	X, m	Y, m
Z, m	0.50	1.29	2.31	3.30		
GS01	-	GD02	GD01	-	1.2	-1.2
GS02	-	GD05	GD04	GD03	0.4	-0.4
GS03	-	GD08	GD07	GD06	-1.8	0.7
GS04	-	GD10	GD09	-	-3.8	0.8

Table 2. Continued

GS05	-	GD12	GD11	-	6.6	-1.9
GS06	-	GD14	GD 13	-	4.9	-0.2
GS07	-	GD21	GD16	GD15	2.3	2.3
GS08	GD22	GD18	GD17	-	-0.2	4.9
GS09	-	GD 20	GD19	-	-2.8	7.4
GS10	-	-	-	-	-	-
GS11	-	GD32	GD31	-	8.4	2.9
GS12	-	GD26	GD25	-	5.6	5.6
GS13	-	GD28	GD27	-	3.9	7.3
GS14	-	GD30	GD29	-	1.0	10.3
GS15	-	GD24	GD23	-	5.8	13.5
GS16	-	GD34	GD33	-	7.3	10.3
GS17	-	GD35	GD36	-	10.7	10.7
GS18	-	GD38	GD37	-	13.7	7.7
GS19	-	GD40	GD39	-	17.1	4.3

2.3.3 2008 LNG Vapor Dispersion Test

Pit 2 (10.06m × 6.4m × 1.22m) filled with water was used to perform the LNG release test, as shown in Fig. 13. The test setup was similar to 2007 test, except the type

of discharge pipe. A 178-mm stainless steel pipe with a 90° bend at the end was made to release LNG. A metal plate was placed under the discharge end to reduce vertical fluid momentum during the release.

Fig. 13. 2008 LNG vapor dispersion test setup

2.3.4 2009 LNG Vapor Dispersion Test

In the recent 2009 field test, 3,000 gallon LNG was spilled on water surface with a rate varying from 80 gpm to 90 gpm. Pit 2 (10.06m × 6.4m × 1.22m) at the BFTF was used to perform this test, as shown Fig. 14. A water pond was created by filling water into the pit to its brim before the test. The large amounts of water below the LNG promoted the vaporization and made the vaporization rate essentially equal to the LNG discharge rate. A fixed 60-m delivery line and a couple of flexible hoses were used to deliver LNG from a road tanker to the target pit. LNG was released via an L-shaped, 4-

inch-diameter stainless-steel discharge pipe. Two foam generators were placed at 4 ft above the ground on one side of the pit as a safety measure in case of any emergency. 4 ft- and 6 ft-high wooden boards were erected in turn around the pit as vapor fences to assess their mitigation effects on vapor cloud dispersion. Photographs of the test setup are shown in Fig. 15

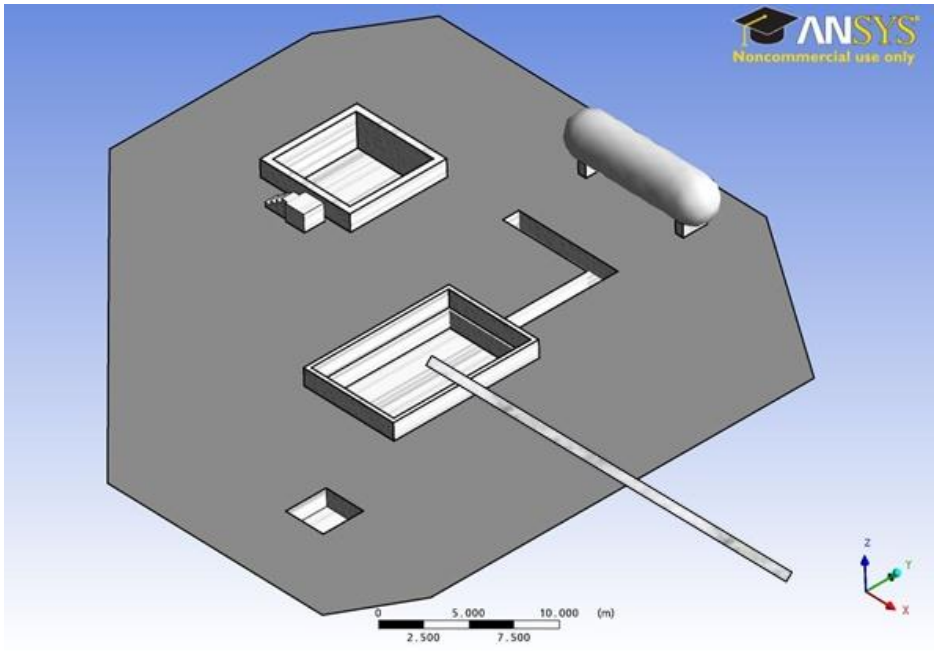

Fig. 14. 2009 LNG vapor dispersion test pit

Fig. 15. Photographs of 2009 LNG vapor dispersion test setup

Four LNG spill and vapor dispersion scenarios were investigated in turn during the test. A summary of these scenarios' parameters is given in Table 3.

Table 3. Summary of scenario parameters in 2009 LNG vapor dispersion test

	Scenario-1	Scenario-2	Scenario-3	Scenario-4
Spill location	0.3 m above water	0.3 m above water	0.3 m above water	0.71 m under water
Starting time	11:44:05	12:04:04	12:22:25	12:42:45
Ending time	11:50:04	12:08:35	12:26:29	12:49:10
Spill duration, s	359	271	244	385
Spill rate, gpm	100*	105	100	15
Spillvolume, gallon	598	474	407	96
Vapor fence, m	1.83	1.2	None	None

Three weather stations were installed in the field at elevations of 10 ft and 33 ft to collect weather information including wind direction, wind speed, humidity, temperature and pressure. Thermocouples were installed both inside the water and at different levels above the water to measure the temperature variations of water body and the vapor cloud emanating from the LNG pool. Another array of thermocouples was placed on the water surface to estimate the LNG pool area during the test. Two types of anemometers were employed above the water to detect the velocity fluctuations in three directions within the vapor fence. Gas detectors were installed at different downwind locations to record the gas concentration and a humidity probe was placed downwind to measure relative humidity of the vapor cloud. The locations of gas detectors are shown in Fig. 16.

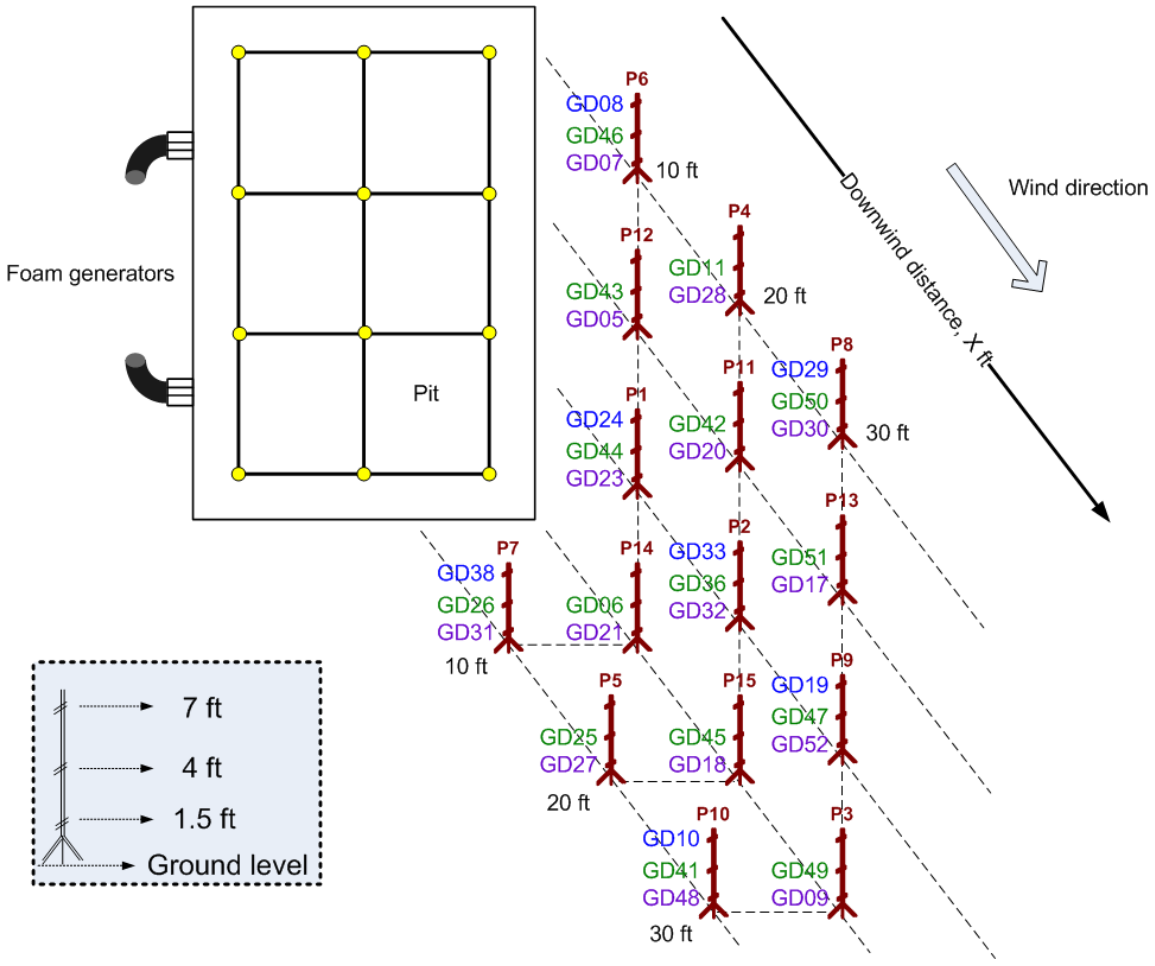

Fig. 16. Gas detectors setup in 2009 LNG vapor dispersion test

In addition, an aluminum discharge pipe with a diameter of 1 inch was placed 2'4'' deep below the water surface for an LNG underwater release test, which is shown in Fig. 17.

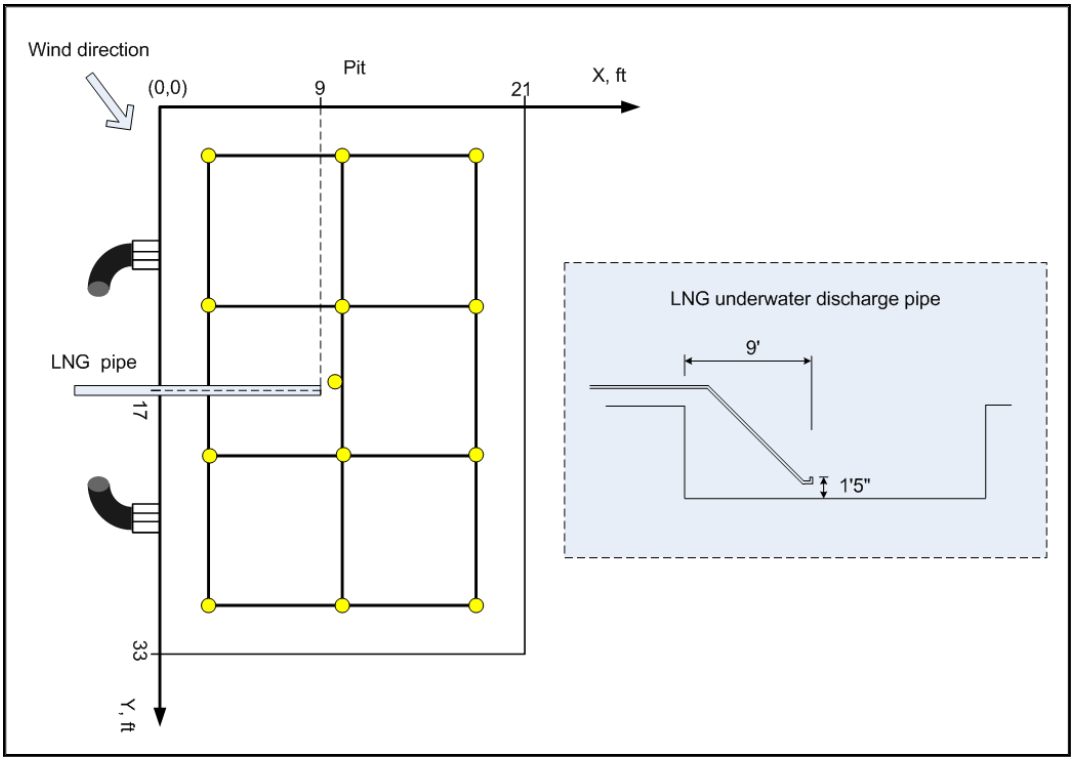

Fig. 17. LNG underwater discharge pipe setup

2.4 Important Observations and Findings

2.4.1 Cloud Visibility

When LNG leaks from containment, a boiling pool forms on the spill surface (water or concrete). A cold fog-like cloud emanates from the pool and drifts downwind as a dense gas. The LNG vapor cloud is visible because of condensation of the moisture from the ambient atmosphere, i.e. the temperature of the vapor/air mixture is below its dew point. However it is inaccurate to estimate the region of flammable hazard only by the visible boundary of the vapor cloud; in reality the hazard may extend beyond this. Fig. 18 shows analogous video images of an LNG vapor cloud recorded at the same time with both a normal camera and a hydrocarbon camera. The white contour of the gas

concentration corresponding to 1% v/v is illustrated. The LFL (4.4%) contour for LNG vapor lies somewhere between the contour illustrated and boundary as observed by the human eye. Pure LNG vapor should be black in the hydrocarbon camera image but water droplets in the vapor cloud affect the color and make it appear greyer.

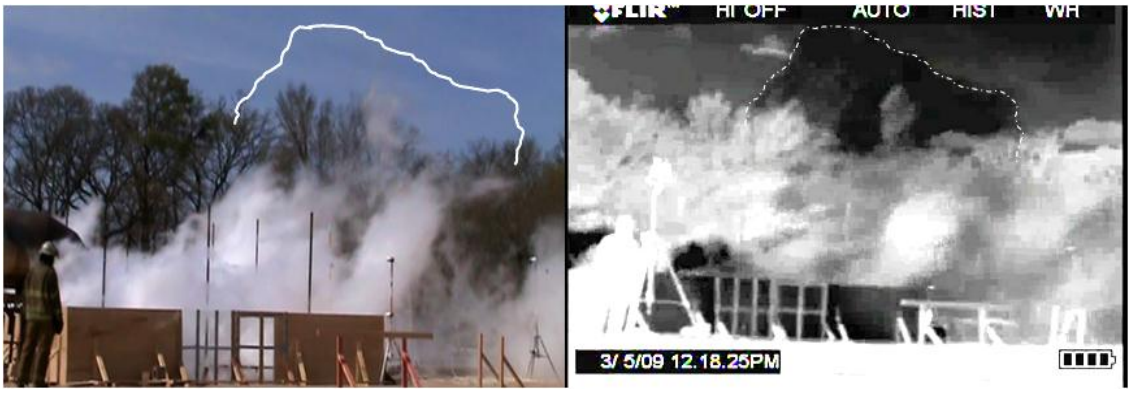

Fig. 18. An LNG vapor cloud image from a normal video (left) and from a hydrocarbon camera video (right)

2.4.2 The Effect of Vapor Fences

Vapor fences can significantly reduce the hazardous downwind distance of a dispersing flammable vapor cloud but they have little effect at shorter distances because of the slumping nature of the cold LNG vapor. The fences can hold up, or retain, the vapor cloud and enhance its positive buoyancy before it starts to become entrained by the wind. They also induce recirculation and promote turbulence to dilute the vapor cloud within the confined source area. Table 4 shows the comparison of turbulence intensity at the 0.91 m level above of the LNG pool surface both with and without a surrounding 1.2 m vapor fence. The turbulence intensities are calculated based on vapor velocity versus time recordings from a three-dimensional sonic anemometer and verified by independent measurements from an adjacent 3-D mechanical anemometer.

Table 4. Turbulence intensities in the LNG source with and without vapor fences

Measured data	With 1.2 m fence	With no fence
Spill duration, s	581	477
Local mean velocity, m s^{-1}	0.56	1.8
Turbulence intensity, %	114	57

2.4.3 LNG Vapor Temperature

Fig. 19 shows the temperature measurements at 7.6 cm and 68.6 cm above the center of the LNG pool for an LNG release onto water starting at time zero and with a duration of 518 seconds. The initial temperature of the LNG vapor will be around -163 °C. The minimum temperatures at the above mentioned locations are -33.8 °C and -12 °C respectively.

The observation that both temperatures start to rise after approximately 420 seconds is interesting but the cause is unclear. One possible explanation is that after this time, significant ice forms on the surface of the water and that as a consequence the LNG vapor production rate is reduced. What is clear is that the LNG vapor has mixed with air and warmed quickly immediately after emanating from the pool.

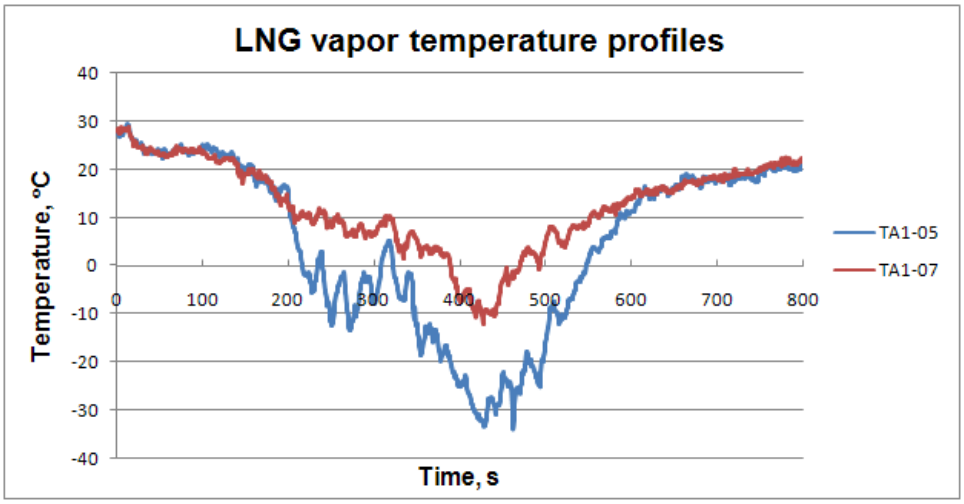

Fig. 19. Temperature profiles at 7.6 cm (TA1-05) and 68.6 cm (TA1-07) above the center of the LNG pool

2.4.4 Ice Formation

The release of LNG onto confined water obviously leads to a decrease of the surface temperature of the water and, if sustained, local freezing. Small amounts of ice formation were observed scattered on the water surface, as shown in Fig. 20.

Fig. 20. Ice formation on the water at the end of the LNG spill test

Amount of ice increasing progressively during the LNG release resulted in a consequent fall in the LNG vaporization rate due to the reduction in temperature difference between the LNG pool and the underlying ice/water mixture. This reduction will probably eventually lead to the cessation of film boiling and thus alter the heat transfer mechanism.

3. SOURCE TERM STUDY ON LNG UNDERWATER RELEASE

3.1 Background

Substantial quantities of liquefied natural gas (LNG) are transported in large, double-hulled, ocean-going vessels. The potential for accidental release of LNG from these vessels is extremely low; however, there have been studies reviewing the vulnerability of the vessels to acts of sabotage and terror leading to puncture of the hulls and release of LNG [1]. One of the scenarios considered is the release of LNG underwater. A symposium held to discuss the knowledge related to LNG pool fire modeling concluded that little was known about the behavior of LNG when released underwater [4]. A recent application filed with the Federal Energy Regulatory Commission (FERC, Docket # CP-04-36-005), for a permit to transport LNG from an offshore LNG ship berth to an on-shore storage and processing terminal included an insulated stainless steel pipe-in-pipe system to be buried under a riverbed in Mt. Hope Bay. The regulatory agency, US Department of Transportation (DOT), has expressed concern over possible LNG leaks from this pipeline into the water column and has indicated that current models are not sufficient to quantify the potential hazards from such leaks [36]. To address this concern, Raj and Bowdoin proposed a theoretical model to describe the various phenomena that occur when LNG is released underwater [37]. Information in the literature on experimental studies of LNG underwater release is scarce. Only two field-scale tests have been reported, and experimental data from these two tests are very limited.

The US Bureau of Mines conducted a single test at a lake near Pittsburg, PA in 1970 with an instantaneous release of 7.7 kg (17 lb) of LNG at a depth of 4.5 m (15 ft) [38]. The National Maritime Institute performed another test at Maplin Sands, England with sponsorship from Shell in 1980, which involved the continuous release of LNG into the sea at a rate of 4.1 m^3/min (1100 gpm) for about 4 minutes from a 0.2 m- (8 inch-) diameter pipe whose end was located about 0.3 m below the water level [39]. In both tests neither LNG pool boiling on the water surface nor a telltale white visible vapor cloud was observed. The absence of visible cloud (that would have formed due to condensation of water vapor) in the air at the point of release from the water surface indicated that the temperature of the vapor emanating at the water surface was above the dew point temperature of air, making the vapor buoyant. This vapor, generated from the underwater release of LNG is positively buoyant (with respect to air) natural gas that rises and disperses more or less like a hot thermal plume. No other quantitative data were collected from either of these two experimental works.

It is because of the lack of data in understanding the interaction between LNG and water when LNG is released underwater that the experiment reported as follows was undertaken. The test discussed was part of a larger set of tests related to understanding the effects of LNG release on water, effects of vapor fences, and the dispersion of vapors liberated from LNG evaporation.

3.2 Modeling

A number of tests with similar release situations in other industries were reviewed to investigate the physical mechanism of the injection of a cold liquid in a bulk hot liquid [37]. Based on the data and correlations from the literature, a mathematical model was developed to characterize the physical process and calculate the temperature of vapor emanating from the water surface when LNG is released underwater. The model breaks the entire underwater physical process into four stages; the different stages discussed in the Raj-Bowdoin model are, in brief, as follows [37].

3.2.1 LNG Jet

The LNG jet outflow velocity from the orifice is given by

$$U_J = \frac{\dot{V}_J}{\frac{\pi}{4} {d_J}^2} \tag{11}$$

where U_J is the jet outflow velocity, $\dot{V}_J$ is the volumetric flow rate, and d_J is the diameter of the jet at the outlet of the orifice (assumed to be equal be the diameter of the orifice).

3.2.2 Liquid Droplets Formation

The vertical distance from the outlet to where the jet completely breaks down into droplets is determined by

$$S_1 = 10 \times d_J \tag{12}$$

Here, S_1 is the vertical distance where the jet completely breaks down into droplets.

The maximum liquid droplet size resulted from the break-up of the jet due to mechanical forces is determined by the following correlations from the literature.

When $Bo_J \leq \pi^2$

$$\frac{d_P}{d_J^{'}} = 3^{1/3}\left(\frac{\rho_J}{\rho_W}\right)^{2/9}\left[\frac{1}{\beta\sqrt{2\pi We_J}} + \frac{2^{7/2}\pi^{3/2}}{\beta We_J\sqrt{L_{PJ}}}\right]^{2/9} \tag{13}$$

When $Bo_J \geq \pi^2$

$$\frac{d_P}{d_J^{'}} = 3^{1/3}\left(\frac{\rho_J}{\rho_W}\right)^{2/9}\left[\frac{1}{\beta\sqrt{2\pi We_J Bo_J}} + \frac{2^{7/2}\pi^{3/2}}{\beta We_J\sqrt{L_{PJ}}}\right]^{2/9} \tag{14}$$

where

$$Bo_J = \frac{g\,(\rho_W - \rho_J)d_J^{'2}}{\sigma_J}, \quad Re_J = \frac{U_J d_J^{'}}{v_J}, \quad We_J = \frac{\rho_J U_J^2 d_J^{'}}{\sigma_J}, \quad L_{PJ} = \frac{Re_J^2}{We_J},$$

$$d_J^{'} = d_J \qquad if \quad d_J \leq \frac{\pi\sigma_J}{g(\rho_W - \rho_J)},$$

$$d_J^{'} = \frac{\pi\sigma_J}{g(\rho_W - \rho_J)} \qquad if \quad d_J \geq \frac{\pi\sigma_J}{g(\rho_W - \rho_J)},$$

where d_P is the maximum diameter of the liquid droplet formed, d_J' is the effective diameter of the jet, g is the acceleration due to gravity, Bo_J is the jet Bond number, Re_J is the jet Reynolds number, We_J is the jet Weber number, Lp_J is the jet

Weber-Reynolds number, ρ_W is the density of water, ρ_J is the density of the jet liquid, σ_J is the surface tension of the jet liquid and β is a constant (0.3).

3.2.3 Liquid Droplets Rising and Vaporization

The calculation of the heating of liquid droplets using the largest size is conservative because the smaller droplets heat up faster. The laminar rise terminal velocity of the largest size is given by

$$U_d = \frac{g(1-\frac{\rho_L}{\rho_W})d_P^2}{18\nu_W} \tag{15}$$

And the turbulent rise velocity is given by

$$U_d = \sqrt{\frac{4}{3}\left[\frac{g(1-\frac{\rho_L}{\rho_W})d_P}{C_D}\right]} \tag{16}$$

Here, U_d is the liquid droplet rise velocity, ν_W is the kinematic viscosity of water and C_D is the drag coefficient on a spherical drop (0.44).

The rate of decease of the liquid droplet diameter is given by

$$\frac{d(d_P)}{dt} = -\frac{2h_{FB}(T_w - T_{sat})}{\lambda\rho_L} \tag{17}$$

where h_{FB} is the film boiling heat transfer coefficient, T_w is the temperature of water, T_{sat} is the saturation temperature of LNG, λ is the heat of vaporization of LNG, and ρ_L is the density of LNG.

Because the diameter decreases linearly with time, the complete evaporation time can be determined by

$$t_{evap} = \frac{\lambda \rho_L d_P}{2h_{FB}(T_W - T_{sat})} \tag{18}$$

Here, t_{evap} is the time to evaporate the largest droplet.

The vertical distance traveled by the largest liquid droplet before it completely evaporates is given by

$$S_d = \left({}^{1}/_{3}\right) U_d \, t_{evap} \tag{19}$$

where, S_d is the vertical distance traveled by the liquid droplet before it completely evaporates.

3.2.4 Vapor Rising and Heating

The temperature of the vapor bubbles is calculated as a function of depth using the following equation.

$$\frac{d\theta}{d\eta} = -\Gamma \sqrt{\frac{(1+P^*)^{\theta}}{(1+P^*\eta)}} (\theta_W - \theta) \tag{20}$$

where

$$\theta = {}^{T}/_{T_i}, \qquad \theta_W = {}^{T_W}/_{T_i}, \qquad \eta = {}^{S}/_{S_i}, \qquad t_{ch} = \frac{S_i}{U_i} = \frac{S_i}{1.74\sqrt{g' d_i}},$$

$$t_{ch,T} = \frac{m_i C_p T_i}{\pi d_i^2 h T_i}, \qquad \Gamma = \frac{t_{ch}}{t_{ch,T}}, \qquad g' = g\left(1 - \frac{\rho_g}{\rho_w}\right), \qquad P^* = \frac{\rho_w g S_i}{P_a},$$

where θ is the dimensionless vapor temperature with respect to initial temperature, T is the temperature of vapor in the bubble at any time, T_i is the initial temperature of vapor in the bubble, θ_W is the dimensionless water temperature with respect to initial temperature, η is the dimensionless depth, S is the depth at any time, S_i is the initial depth where the bubble is formed, t_{ch} is the characteristic rise time, U_i is the initial terminal velocity of rise of the bubble, g' is the effective acceleration due to gravity, d_i is the diameter of the vapor bubble at depth S_i, $t_{ch,T}$ is the characteristic heat transfer time, m_i is the initial mass of vapor in the bubble, C_p is the specific heat of vapor at constant pressure, h is the water to vapor bubble overall heat transfer coefficient, Γ is the ratio of characteristic rise time to heat transfer time, ρ_g is the density of vapor in the bubble, P* is the dimensionless maximum hydrostatic pressure, and P_a is the atmospheric pressure.

3.3 Test Setup Description

The test presented in this work was conducted at the Brayton Fire Training Field, Texas Engineering Extension Service, Texas A&M University System, College Station, TX. The test setup consisted of a concrete pit (10.06 m x 6.4 m x 1.22 m) filled with municipal water to a depth of 1.14 m. LNG was discharged vertically from a 2.5 cm-diameter nozzle located at a depth of 0.71 m below the water surface. The LNG discharge pipe, with a nozzle at its end, is shown in Fig. 21. Further details of the test conditions are reported in Table 5. The LNG (99.8% liquefied methane) stored in a road transport (located about 50 m from the pit) was conveyed to the pit in a 10-cm diameter

insulated pipe and was discharged under the pressure built up in the transporter tank. The discharge rate was measured by an in-line LNG turbo flow meter close to the transporter. Schematic plan and cross-sectional views of the test pit are shown in Fig. 22.

Fig. 21. LNG discharge pipe side view (left) and top view (right)

Table 5. Underwater LNG release test conditions*

Parameter	**Parameter Values**			
Pit dimensions (L x W x D)	10.06 x 6.4 x 1.22	m	33 x 21 x 4	ft
Water depth at full fill	1.14	m	3’ 9”	ft
Discharge section height above the pit bottom	0.432	m	1’ 5”	ft
Discharge pipe outlet diameter	2.54×10^{-2}	m	1	in
Orientation of LNG discharge	Vertically up through the water column			

Table 5. Continued

Parameter	**Parameter Values**			
Coordinate of the release point with respect to the ground level upwind corner of the pit (L x W x D)	4.72 x 1.83 x 0.79	m	15.5 x 6 x 2.58	ft
Depth of exit section of discharge pipe below the water surface	0.71	m	2' 4"	ft
Volume rate of LNG discharge	(40.5 ± 13.4) x 10^{-3}	m^3/min	10.7 ± 3.55	gpm
Total duration of test	330	s	5.5	min
Volume of water in the pit	73.6	m^3	2600	cft
Nominal wind direction	Along the diagonal of the pit			
Wind speed	2.7 ± 1.1	m/s	6.1 ± 2.5	mph
Water Temperature	16 ± 0.4	^oC	61.5 ± 0.7	^oF
Atmospheric Temperature	9.0	^oC	47.6	^oF
Relative Humidity	52.1	%	52.1	%
Dew point Temperature	- 0.4	^oC	29.6	^oF

* Test was conducted at the Brayton Fire Training Field, Texas Engineering Extension Service, Texas A&M University System, 1595 Nuclear Science Road, College Station, TX 77843-8000

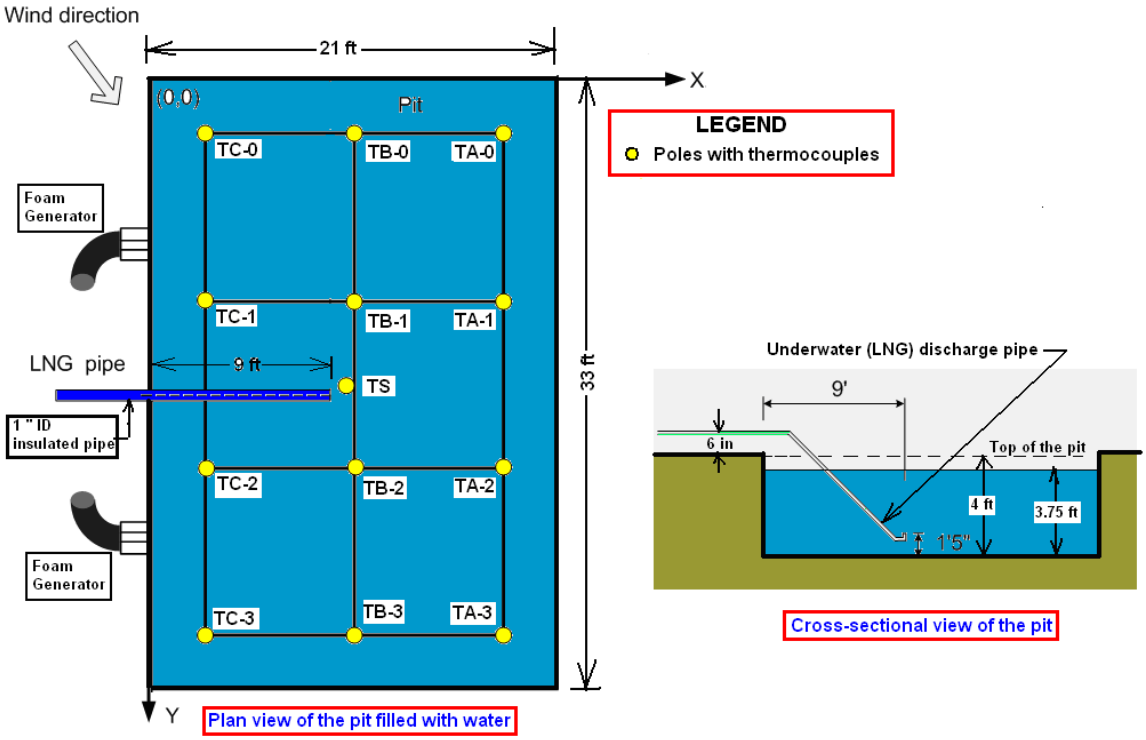

Fig. 22. Plan and cross sectional view of water filled test pit showing the locations of the LNG discharge pipe and thermocouple poles

A single waterproof video camera whose focal length could be varied from a remote location was placed underwater near one wall of the pit. Two fixed digital video cameras were located on land to obtain a crosswind view of the dispersing vapor. One digital video camera was hand-held and was moved during the test to obtain optimal views of the test results. A number of thermocouples were provided on poles located inside the pit. These thermocouples measured both the water temperature (at several depths) and the temperature above the water surface (air or vapor temperatures) at various locations. The pole positions and thermocouple locations are shown schematically in Fig. 23. Also provided within the pit area were gas sensors to record gas

concentrations over the pit. These are indicated in Fig. 24. Several gas sensors, at different heights above ground, were located downwind of the pit on poles positioned at various distances (both downwind and cross wind) from the pit. These arrangements are shown schematically in Fig. 25. In addition to the above instrumentation, the meteorological conditions during the test were recorded, close to and upwind of the test pit, using a "Vantage Pro" weather station. The data from all gas sensors, thermocouples, and the LNG flow meter were recorded every second on a central data acquisition system and transferred to a laptop computer for storage. The weather data from the meteorological station were recorded every minute. Table 6 lists the quantities and specifications of the sensors and instruments used in the test.

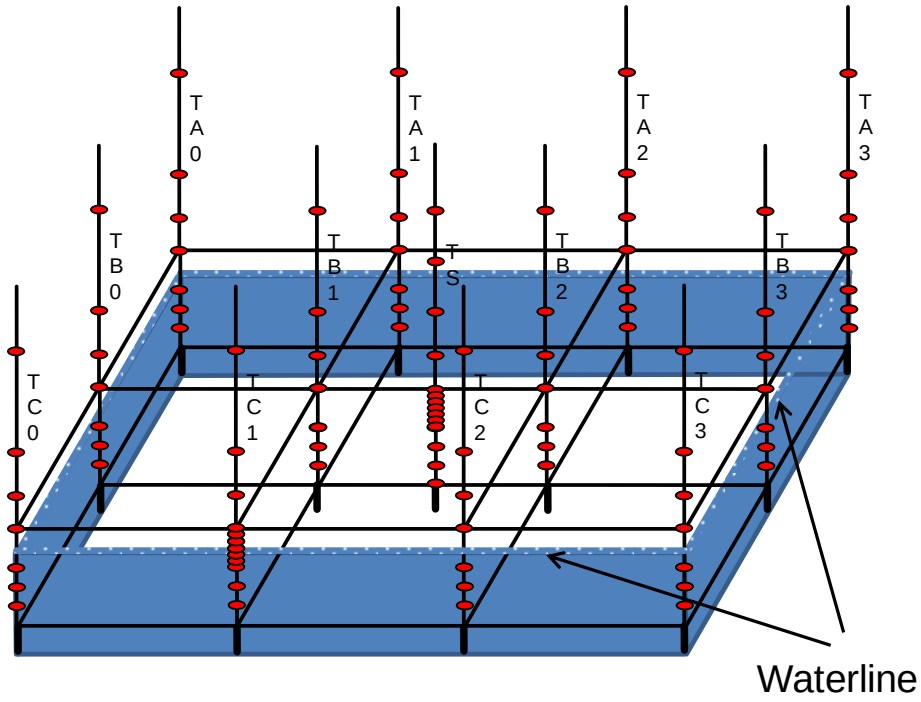

Fig. 23. Details of thermocouple locations on poles within the test pit

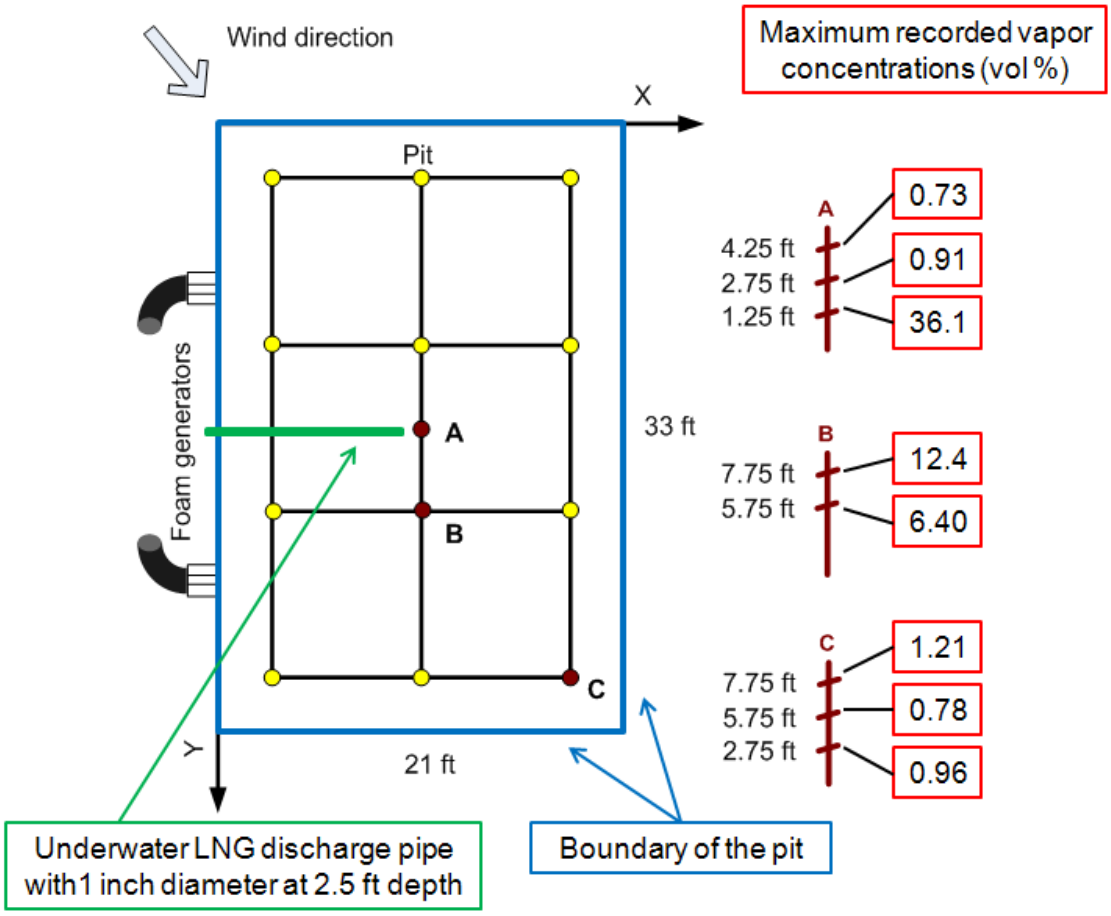

Fig. 24. Locations of gas concentration sensors on poles in the pit and the maximum recorded vapor concentrations

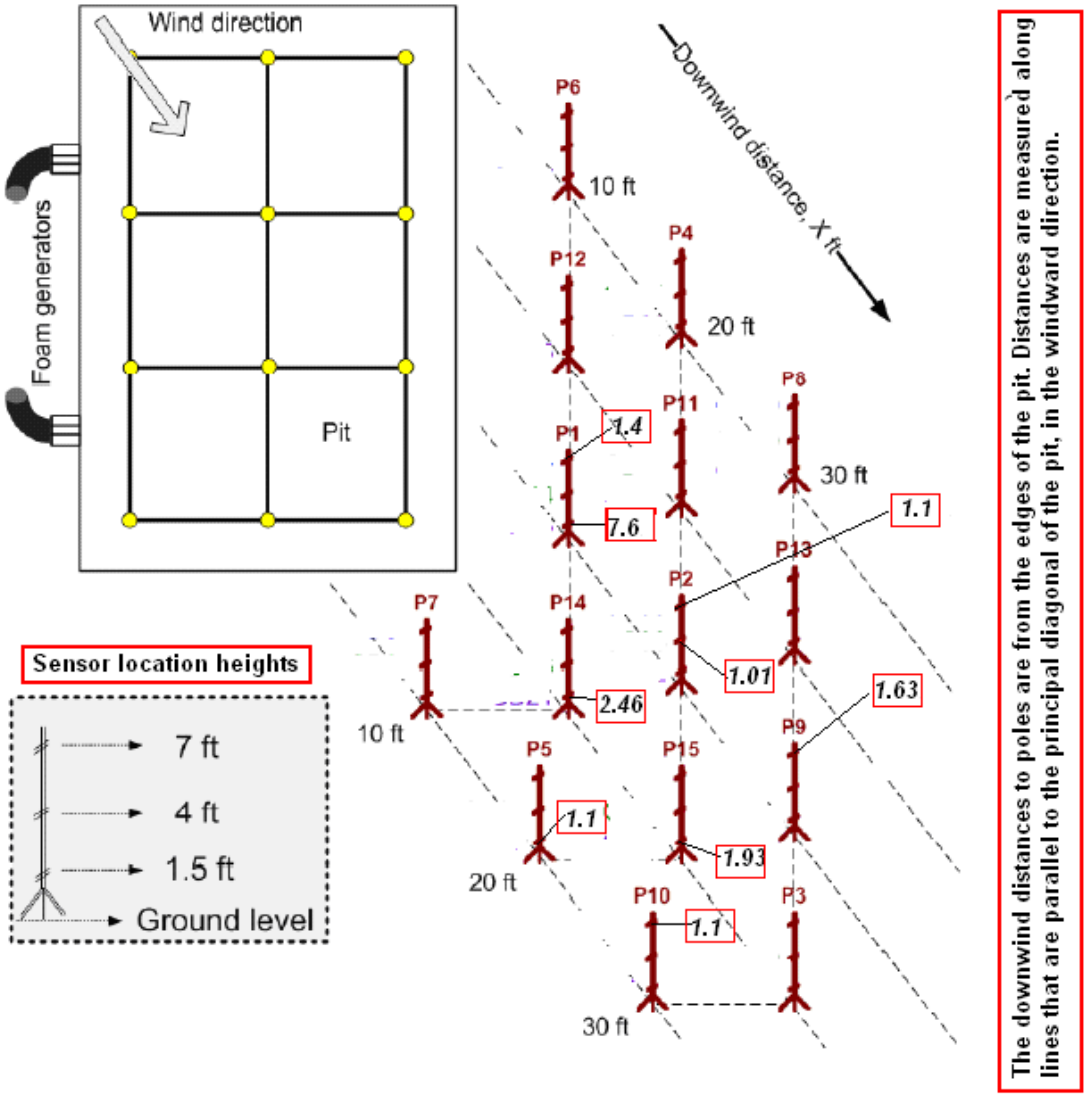

Fig. 25. Gas concentration sensors on poles downwind of the pit and measured peak concentrations values (vol %)

Table 6. List and specifications of the instruments used in the test

Instrument	Quantity	Specifications	Supplier
Thermocouple	116	K-type thermocouples	Omega
Gas sensor	40	Searchpoint Optima Plus Point Infrared Gas Detectors	Honeywell Analytics
	6	Impact Pro Multi-Gas Detectors	
	6	MiniMax X4 Multi-Gas Detectors	
Flow meter	1	Turbine cryogenic flow meter	Omega
Weather instrument	1	Vantage Pro 2 weather station	Davis instruments

The test procedure consisted of opening the main valve on the transporter and allowing the LNG (or liquefied methane) to flow into the transfer pipe to cool it. The transfer pipe had a valve very close to the pit, and after sufficient cooling of the transfer pipe (this took about 15 to 20 minutes) the valve was opened to let LNG discharge through the nozzle underwater. The extent of valve opening previously calibrated to deliver LNG at the desired flow rate. The overall duration of the test was about 6.5 minutes.

3.4 Results and Discussions

The various data obtained in the single test of underwater LNG release are shown in Fig. 24 though Fig. 29. The data from the LNG flow meter is plotted in Fig. 26 as a function of time. An initial very high spike can be seen within the first 2 or 3 seconds which was attributed to the flow of LNG vapor in the pipe due to evaporation. This was followed (for approximately the next 90 seconds) by what appeared to be a two-phase flow in the pipe, near the flow meter. The readings during these two periods were not accurate because the flow meter was not designed for gas flow measurement or two-phase flow measurement. The average of the flow data between 85 s and 310 s is to be viewed as representing the liquid methane (LNG) flow rate. The data statistics indicate that the flow rate was 40.5 ± 13.4 Lpm (10.7 ± 3.55 gpm).

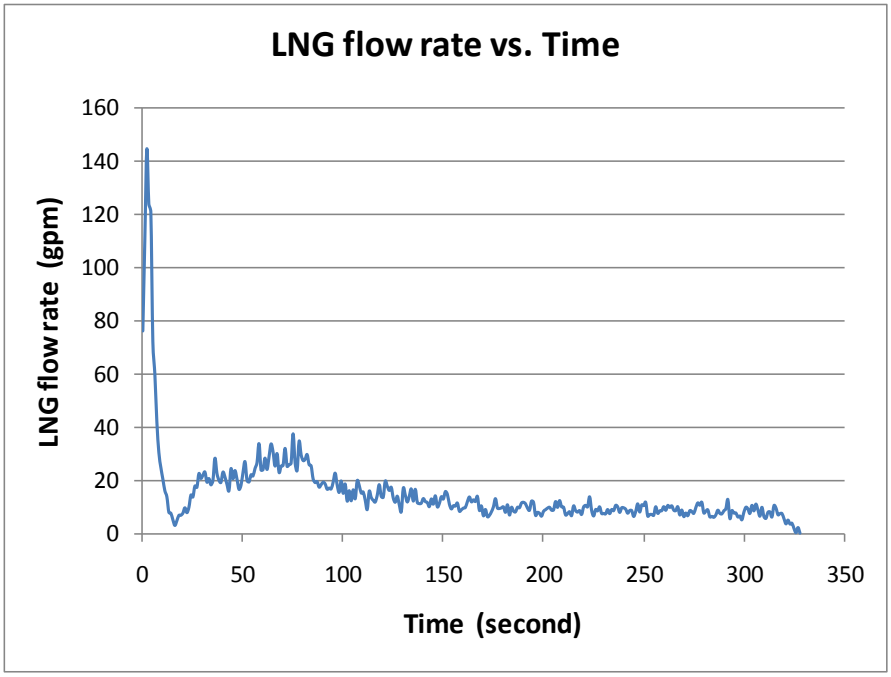

Fig. 26. LNG flow rate as a function of time measured by an in-line turbine flow meter

Observations during the test, based on the underwater video camera recording, indicate the presence of a dark vertical conical plume. It was not possible to distinguish between the liquid jet, liquid droplets and vapors in this plume. It was seen, however, that the flow was pulsating and resulted in the formation of a series of, what looked like, mushroom clouds with long tails, that rapidly moved up to the water surface. Over-the-land video camera images focused on the water surface did not reveal the formation or presence of any LNG pool floating and evaporating on the water surface. Despite the fact that the water volume in the pit was about 300 times the volume of LNG released, the water surface was agitated significantly. This may have been due to the violence of the vertical liquid jet flow and the possible effects of high rates of evaporation and large volume rates of gas release.

Fig. 27A and 27B show photographs from the underwater video camera. In Fig. 27A the flow at early stages of release (in the first 200 seconds) is shown. The outflow from the nozzle likely contained both the LNG liquid and vapor generated within the discharge pipe (due to the heat transfer from the warm pipe to flowing LNG). This figure clearly shows the shattering of the LNG contained in the released flow. The intermittent nature of the flow is clearly seen in the formation of two distinct “mushroom” clouds, one fully developed and the other incipient at the nozzle. In Fig. 27B, the discharge end of the pipe with the nozzle was pushed down towards the pit floor by the momentum of the exiting liquid jet. Also, the liquid jet flow out of the nozzle looks very dark and is in the form of the classic mushroom cloud with a tail. Because of the shallow release depth, it is possible that the entire liquid released in the jet was not totally vaporized within the

water column but a part of the liquid was thrown up into the air (in the form of liquid droplets) along with the generated vapors. Thus, “geysering” of the liquid/vapor discharge at the water surface was observed. The vertical momentum of the jet at release may not have been completely destroyed by the time the liquid/vapor combination reached the water surface. This phenomenon agreed with the prediction results on liquid droplets characteristics based on the Raj-Bowdoin model described in section 3.2. As shown in Table 7, the calculated vertical distance where the jet completely breaks down into droplets was 0.254 m and the vertical distance traveled by the largest liquid droplet by the time of complete evaporation was 0.934 m. Therefore, the total vertical distance from the outlet to where the largest liquid droplets completely evaporated was 1.188 m, which was larger than the release depth (0.71m). This indicates that when LNG rose to the water surface, a small fraction was still in the form of liquid droplets and thus thrown out of water due to the vertical momentum.

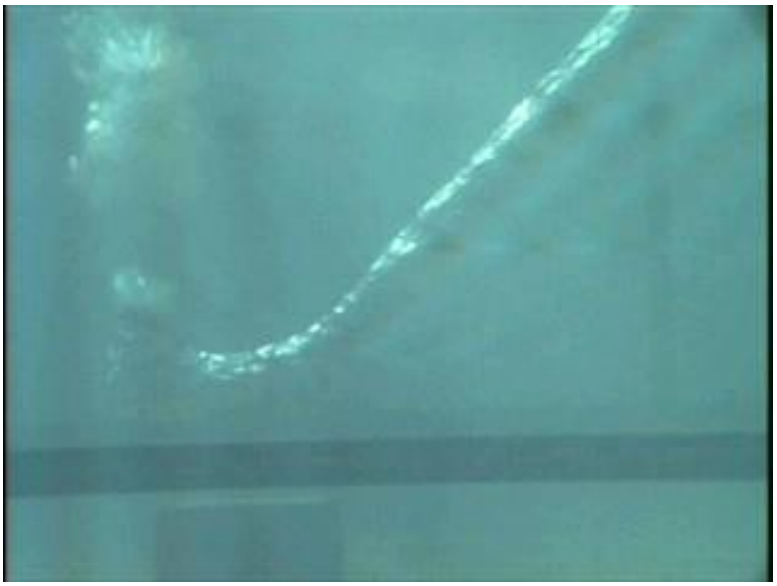

Fig. 27A. A snap-shot at an early time during underwater release when the flow out of the nozzle included both LNG liquid and vapor generated in the pipe

Fig. 27B. A photograph of a later time underwater release of LNG. Very likely only LNG liquid is being released from the nozzle

Table 7. LNG liquid droplets characteristics calculation results

Parameter	Symbol	Value	Unit
Jet diameter at the outlet of the orifice	d_J	0.0254	m
Jet outflow velocity	U_J	1.33	m/s
Vertical distance where the jet completely breaks down into droplets	S_1	0.254	m
Effective jet diameter	d_J'	0.00487	m
Maximum size of liquid droplet formed	d_p	0.00335	m
Liquid droplet rise velocity (laminar)	U_d	0.593	m/s
Time to evaporate the largest droplet	t_{evap}	4.72	s
Vertical distance traveled by the liquid droplet before it completely evaporates	S_d	0.934	m

Note: Results in this table were obtained by applying the Raj-Bowdoin model to the conditions of this test.

A white vapor cloud emanated from the water surface and was observed with tendency to rise straight up, except when the wind velocity was high. The wind velocity during the test was relatively stable 2.7 ± 1.1 m/s (6.1 ± 2.5 mph) except when it gusted. Fig. 28 compares photographs of the white vapor cloud (formed by condensation of atmospheric water vapor in the air and emanating vapor mixture) seen from the crosswind side of the pit under two different release conditions. For LNG underwater release, shown in Fig. 28(A) the white cloud rose vertically and became tilted at a certain

height by the prevailing wind. The visibility of the cloud indicates that the vapor emanating from the water surface was at a lower temperature than the dew point of the atmospheric air (Air temperature and relative humidity were respectively 9 ^{o}C and 52.1 %. The corresponding dew point temperature is – 0.4 ^{o}C). The temperature at which the density of natural gas equals that of the ambient air (under test conditions) is – 117 ^{o}C (-179 ^{o}F). Comparison of the vapor plume shape for LNG released underwater with that of LNG released onto water indicates that the vapor temperature was significantly higher than this value (assuming the LNG vapor immediately from the pool floating on the water was approximately -117 °C). This observation is discussed in further detail later in this section. It was also observed by the mobile video camera that liquid droplets were thrown upward sporadically into the visible gas plume. In Fig. 28(B) the vapor cloud formed by the release of LNG onto the water surface (in another test conducted in this series) is indicated. It is clearly seen that the vapor cloud is “heavy” and disperses at ground level.

Fig. 28. Photographs of vapor cloud emanating from the water surface: (A) LNG release underwater, (B) LNG release onto water surface

Fig. 29 shows gas concentration data as a function of time from sensors on poles within the pit and downwind on the ground. Sensors on pole B, which was located to the east of pole A and was in the path of the wind-carried plume, show reasonable values for the concentrations. These concentrations were lower than 15%. Also shown in this figure is the record of the sensor at 1.5 ft height above ground on pole 1, which was almost directly downwind of the pit 10 ft from the edge. The concentration records on poles 5 and 15 ranged from 1% to 2%, both of which were on land 20 ft downwind away from the pit. Fig. 24 shows the maximum concentrations recorded by the sensors on poles A, B and C located in the pit. It is seen that the maximum concentrations on poles B and C were always at the top-most sensor and that the maximum concentration on pole C was less than that on pole B. This indicates that the plume was rising.

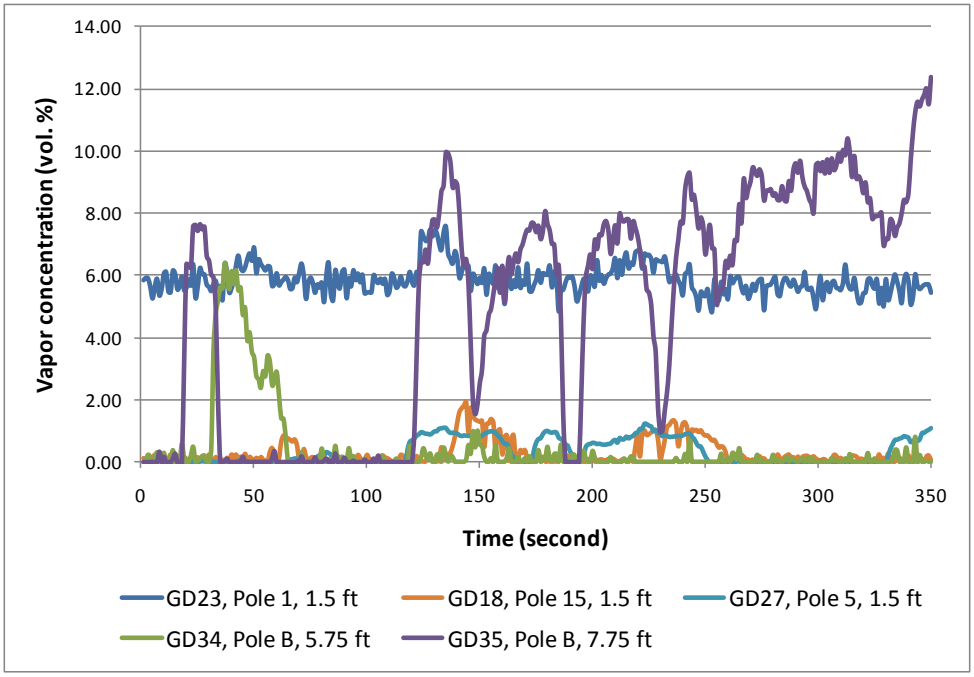

Fig. 29. Vapor concentration as a function of time measured by different sensors

Also shown in Fig. 25 are the maximum concentrations measured by the sensors on poles located downwind on land. It is noted that the peak concentrations shown did not occur at the same time. Although on most of the poles the highest of the peak concentrations appeared to occur on the top-most sensor, there did seem to be some exceptions, namely, pole 1 and pole 14. These anomalies can be attributed to wind gusts when the plume was bent more horizontally. However, it is worth noting that even at 7 ft height most of the poles only registered 1% for the highest concentration. This clearly indicates the rising up-in-the-air nature of the plume. The recorded concentrations may represent the "wing values" of the vertical concentration distribution on a cloud whose centerline was rising as it dispersed downwind.

Fig. 30 shows the lowest temperatures recorded by the thermocouples on poles located inside the pit (no thermocouples were provided on poles on land; hence the data on cloud temperature on land are not available). Most of the minimum temperatures recorded seem to refer to the air temperature (indicating that the plume did not touch these thermocouples). Where the plume may have blown over the thermocouples the minimum temperatures ranged from 5 ^{o}C to -1 ^{o}C (41 ^{o}F to 30 ^{o}F). The lowest recorded temperature by any thermocouple in the pit was -1 ^{o}C (30 ^{o}F). Noting that the neutral buoyancy temperature for natural gas is -117 ^{o}C (- 179 ^{o}F), it is clear that the vapor cloud emanating from the water surface was buoyant. However, the emanating vapor temperature was not the same as, or even close to, the water temperature (16 ^{o}C or 61 ^{o}F). This may have been due to the fact that the vapor generated by LNG vaporization within the water column did not have sufficient time to heat up due to the rather shallow

depth of release. Moreover, the upward pointing liquid jet release imparts vertical momentum to the jet and the jet breakup and vaporization may thus be occurring at shallower depths (of the order of, say, 0.3 m). It is remarkable that even with such shallow depth and high velocity release the emanating vapor is significantly buoyant.

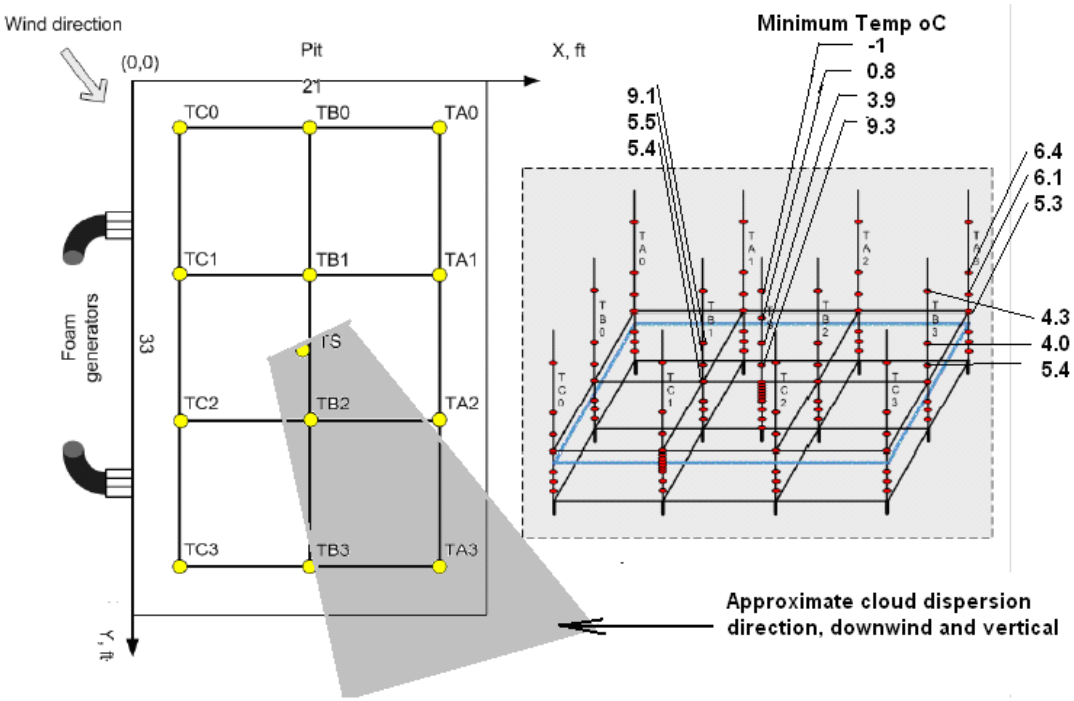

Fig. 30. Minimum vapor temperatures recorded at different locations over the pit during vapor emission from the underwater LNG release

3.5 Principal Findings

- Even under relatively shallow depth below water surface where LNG was released, the vapor cloud formed by the vaporization of LNG underwater was found to be buoyant.
- The temperature of the vapor emanating from the water surface, in the specific test reported, was below the dew point temperature of the atmospheric air, thus making the vapor cloud visible due to condensation of atmospheric water vapor.
- The lowest temperature recorded for the vapor cloud emanating from the water surface when LNG was released underwater was -1 oC (30 oF). This temperature was much higher than the temperature measured at the same position in other tests (conducted in this series) in which LNG was released onto the surface of water. This indicates that an underwater release generated a more buoyant vapor due to very high heat transfer rates from water to LNG droplets (formed by the shattering of the LNG jet) as well as to the vapor bubbles formed.
- The general tendency of the vapor to buoyantly rise and disperse is clearly demonstrated both by video photographs and the concentration measurements by sensors located on poles downwind of the pit. The concentration records on poles on land, even at 7.5 m (25 ft) downwind of the source indicate maximum concentrations ranged from 1% to 2% (except for one record). All

other downwind sensors beyond the first row of poles at 3m from the edge of the pit show even lower concentrations.

- The maximum height of the concentration sensor on poles on land, downwind of the pit, was only 2.1 m (7 ft) above the ground. However, the center line of the visible plume, determined from the video records, was far above this height even for the first row of poles. This observation may explain the fact that the maximum reading of the concentration data obtained from these poles indicated 1% to 2%, indicating that the sensors probably detected only the tail values of the vertical concentration distribution in the buoyant plumes.
- The concentration data obtained from the sensors located on poles within the pit also indicated that rise of the vapor plume in air. These concentration values were higher (as one would expect) than those from the on-land sensors. These values (of vapor concentrations above the water in the pit) were in the 5% to 15% range, which was still considerably lower than those that occur in the case of LNG release onto water surface and the dispersion of vapor produced therefrom.
- No LNG pool was observed on the surface of water at any time during the test.

3.6 Summary

The underwater LNG release test was conducted to understand the phenomena that occur when LNG is released underwater and to determine the characteristic of the vapor emanating from the water surface. Another objective of the test was to determine if an LNG liquid pool formed on the water surface, spread and evaporated in a manner similar to that from an on-the-surface release of LNG.

A pit of dimensions 10.06 m x 6.4 m and 1.22 m depth filled with water to 1.14 m depth was used. A vertically upward shooting LNG jet was released from a pipe of 2.54 cm diameter at a depth of 0.71 m below the water surface. LNG was released over 5.5-minute duration, with a flow rate of 0.675 ± 0.223 L/s. The wind speed varied between 2 m/s to 4 m/s during the test.

Data were collected as a function of time at a number of locations. These data included LNG flow rate, meteorological conditions, temperatures at a number of locations within the water column, and vapor temperatures and concentrations in air at different downwind locations and heights. Concentration measurements were made with instruments on poles located at 3.05 m, 6.1 m and 9.14 m from the downwind edge of the pit and at heights 0.46 m, 1.22 m, and 2.13 m. The phenomena occurring underwater were recorded with an underwater video camera. Water surface and in-air phenomena including the dispersion of the vapor emanating from the water surface were captured on three land-based video cameras.

The lowest temperature recorded for the vapor emanating from the water surface was -1 ^{o}C indicating that the vapor emitted into air was buoyant. In general the

maximum concentration observed at each instrument pole was progressively at higher and higher elevations as one travelled downwind, indicating that the vapor cloud was rising. These findings from the instrument recorded data were supported by the visual record showing the “white” cloud rising, more or less vertically, in air. No LNG pool was observed on the surface of water. A previously published theoretical model was validated against test data.

4. LNG VAPOR DISPERSION MODELING

4.1 Background

As LNG import terminal and facility construction increases, concerns about the potential hazards that LNG spills could pose have been raised. One of the major hazards from an accidental LNG release is the formation of a flammable vapor cloud, which drifts downwind near the ground for a certain time until it completely warms up and dissipates in the atmosphere. If an ignition source is present and vapors mix with air in its flammability range, the vapor cloud will ignite and burn [16]. To ensure public safety in adjacent populated areas, federal regulation 49 CFR Part 193 [40] and standard NFPA 59A [41] have required LNG industries to use validated consequence models to predict potential hazardous areas (exclusion zones) around LNG facilities in the event of an accidental LNG release.

Consequence modeling of accidental LNG releases has been studied extensively as part of an effort extended to prevent and mitigate such incidents. Two types of major LNG vapor dispersion models are integral models and computational fluid dynamics (CFD) models. Integral models are widely used because of their fast computational time and ease of use. However, most integral models have limitations in taking into account the effects of terrain and obstacles in LNG spill scenarios [42]. CFD models are able to provide a detailed description of physical processes and handle complex geometries, and can thus be used to predict the behavior of LNG vapor cloud dispersion in a site-specific risk analysis [43-47]. However, CFD simulation setup methods for LNG vapor

dispersion and their validation against actual large or medium-scale spill tests have not been sufficiently reported in the literature.

In the present work, ANSYS CFX 11.0 was used to perform simulations of LNG vapor dispersion whose results would then be validated with LNG spill experiments at BFTF. Here, we report the important parameters for setting up the LNG vapor dispersion simulation using ANSYS CFX. Essential inputs associated with the domain and boundary conditions are discussed. The quality of the simulation results is always influenced by uncertainties or errors in parameters related to the numerical methods and physical models. Thus, a sensitivity analysis was conducted to illustrate the impact of the mesh size and source term turbulence intensity on predicting safe separation distances (distance to the half lower flammable limit, ½ LFL). The motivation of this work was to provide guidance in modeling LNG vapor dispersion with ANSYS CFX, which can be used to evaluate the design, siting, and layout of LNG plants.

4.2 ANSYS CFX Codes

The ANSYS CFX is a general-purpose CFD package capable of solving diverse and complex three-dimensional fluid flow problems. ANSYS CFX uses the Navier-Stokes equations to describe the fundamental processes of momentum, heat, and mass transfer. It also incorporates a number of mathematical models that can be used together with the Navier-Stokes equations to describe other physical or chemical processes such as turbulence, combustion, or radiation. Like most commercial CFD packages, ANSYS CFX uses a finite volume approach to convert the governing partial differential

equations into a system of discrete algebraic equations by discretizing the computational domain. These equations may result in a solution with specified domain boundary conditions. For a transient simulation, an initial condition is also required to numerically close the equations. One of the most important features of CFX is that it uses a coupled solver, which solves the fluid flow and pressure as a single system and faster than the segregated solver up to a certain number of control volumes, as it requires fewer iterations to achieve equally-converged solutions [48, 49].

In essence, the atmospheric dispersion of LNG vapor is a type of turbulent, buoyant, multi-component fluid flow. In order to understand the physical meaning of various parameters associated with selected models, it is necessary to get familiar with mathematical formulations of the models.

If k-ε turbulence model is employed, the governing Reynolds averaged Navier-Stokes (RANS) equations representing mass, momentum, and heat transfer conservation, include [48, 49]:

The continuity equation

$$\frac{\partial \rho}{\partial t} + \nabla \cdot (\rho \mathbf{u}) = 0 \tag{21}$$

The momentum equation

$$\frac{\partial \rho \boldsymbol{U}}{\partial t} + \nabla \cdot (\rho \boldsymbol{U} \otimes \boldsymbol{U}) = -\nabla p' + \nabla \cdot (\mu_{\text{eff}} \nabla \boldsymbol{U}) + \nabla \cdot (\mu_{\text{eff}} \nabla \boldsymbol{U})^T + B \tag{22}$$

And the energy equation

$$\frac{\partial (\rho h_{tot})}{\partial x} - \nabla \cdot (\rho \boldsymbol{U} h_{tot}) = \frac{\partial p}{\partial t} + \nabla \cdot \left(\lambda \nabla T + \frac{\mu_t}{Pr_t} \nabla h \right) + \nabla \cdot (\boldsymbol{U} \cdot \tau) + S_E \tag{23}$$

where

$$\mu_{\text{eff}} = \mu + \mu_t \tag{24}$$

$$\mu_t = C_\mu \rho \frac{k^2}{\varepsilon} \tag{25}$$

$$p^{'} = p_{\text{stat}} + \frac{2\rho k}{3} \tag{26}$$

B is the sum of body forces, μ_{eff} is the effective viscosity, μ_t is the turbulence viscosity, C_μ is the constant, p' is the modified pressure, and Pr_t is the turbulent Prandtl number.

Here, the k-ε model introduces two new variables into this system of equations: k-turbulent kinetic energy and ε-turbulent dissipation rate, which are given by:

$$\frac{\partial(\rho k)}{\partial t} + \nabla \cdot (\rho \boldsymbol{U} k) = \nabla \cdot \left[\left(\mu + \frac{\mu_t}{\sigma_k}\right) \nabla k\right] + P_k - \rho\varepsilon \tag{27}$$

$$\frac{\partial(\rho \varepsilon)}{\partial t} + \nabla \cdot (\rho \boldsymbol{U} \varepsilon) = \nabla \cdot \left[\left(\mu + \frac{\mu_t}{\sigma_\varepsilon}\right) \nabla \varepsilon\right] + \frac{\varepsilon}{k}(C_{\varepsilon 1} P_k - C_{\varepsilon 2} \rho \varepsilon) \tag{28}$$

where

$$P_k = \mu_t \nabla \boldsymbol{U} \cdot (\nabla \boldsymbol{U} + \nabla \boldsymbol{U}^T) - \frac{2}{3} \nabla \cdot \boldsymbol{U}(3\mu_t \nabla \cdot \boldsymbol{U} + \rho k) + P_{kb} \tag{29}$$

$C_{\varepsilon 1}$, $C_{\varepsilon 2}$, σ_k and σ_ε are all constants, P_k is the turbulence production due to viscous and buoyancy forces, and P_{kb} is the turbulence production due to buoyancy forces.

If full buoyance model is selected, P_{kb} is calculated through

$$P_{kb} = \frac{\mu_t}{\rho \sigma_\rho} \boldsymbol{g} \cdot \nabla \rho \tag{30}$$

In a multi-component fluid system, additional equations have to be solved to determine how components of the fluid are transported in the system.

$$\frac{\partial(\bar{\rho}\,\tilde{Y}_i)}{\partial t} + \frac{\partial(\bar{\rho}\,\tilde{U}_j\,\tilde{Y}_i)}{\partial x_j} = \frac{\partial}{\partial x_j}\left(\left(\Gamma_i + \frac{\mu_t}{Sc_t}\right)\frac{\partial \tilde{Y}_i}{\partial x_j}\right) + S_i \tag{31}$$

where

$$\tilde{Y}_i = \frac{\tilde{\rho}_i}{\bar{\rho}} \tag{32}$$

$\tilde{\rho}_i$ is the mass-average density of fluid component i in the mixture, $\bar{\rho}$ is the density of the mixture, $\tilde{Y}_i$ is the mass fraction of component i, Γ_i is the molecular diffusion coefficient, Sc_t is the turbulent Schmidt number, and *Si* is the source term for component *i* which includes the effects of chemical reactions.

4.3 Simulation Setup with ANSYS CFX

The basic procedure in modeling LNG vapor dispersion with ANSYS CFX consists of five steps—creating the geometry, meshing, pre-processing, solving, and post-processing. With regards to simulation setup, only the first three steps are considered. Table 8 lists all the essential inputs or parameters in the setup process. Details of the inputs in Table 8 are described in the following sections.

Table 8. Summary of input variables for LNG vapor dispersion simulation setup

Components	Inputs (Parameters)
Geometry creation	3-D geometry (terrain and obstacles)
Meshing	Mesh shape and size
Preprocessing-domain	Fluid properties
	Turbulence model
	Heat transfer model
	Buoyancy model
Preprocessing-Atmosphere boundary	Fluid composition
	Wind direction and velocity profile
	Temperature profile
	Turbulence profile
Preprocessing-LNG pool boundary	Fluid composition
	Vapor evaporation velocity
	Vapor temperature
	Turbulence
Preprocessing-Ground boundary	Influence on flow
	Surface roughness height
	Surface temperature or heat flux

4.3.1 Creating Geometry

The first step in a CFD simulation is to create the geometry of the flow field. The flow field of interest is represented by a computational domain within which the equations of fluid flow and heat transfer are solved. Considering one of the primary advantages of CFD models is that it is capable of handling complex geometries, the appropriate geometry must be built or imported to represent the features of flow field that impact the simulated variables of interest. When modeling LNG vapor dispersion, obstacles and terrain near the source or in the traveling path of the LNG vapor downwind must be constructed in the domain to account for their effects on the vapor cloud; otherwise, the CFD analysis may overestimate or underestimate the hazardous area. Some geometries can contribute to an increase in vapor concentrations by lowering the wind speed or decreasing the atmospheric turbulence, while others can reduce the downwind vapor concentrations by trapping the vapor within the source area or diluting in the turbulent wake of obstacles [50].

4.3.2 Meshing

The second step is subdividing the computational domain. The domain is discretized into a number of small control volumes using a mesh generated by CFX-Mesh. The mesh had structured grids in the near-wall regions and unstructured grids in the bulk of domain, which contains tetrahedral, pyramid and prismatic elements. ANSYS CFX provides a list of criteria to assess the quality of the mesh through mesh-associated parameters such as the edge length ratio, maximum and minimum face angle,

connectivity number, and element volume ratio [51]. The mesh size must be chosen carefully to avoid adverse effect on the simulation accuracy. A recommended approach to eliminate mesh size influence is to seek mesh-independent solutions by testing with gradually-reduced mesh sizes until the simulation results no longer change [52-54].

4.3.3 Domain and Boundary Conditions

4.3.3.1 Domain

ANSYS CFX is not designed especially as a consequence model for LNG spill hazards, and therefore fluid properties and physical models must be identified to characterize the physical process of LNG vapor dispersion when defining the domain. Detailed explanations and the selection of these properties are described as follows.

LNG is mainly composed of methane, but may also contain small amounts of ethane, propane, and heavier hydrocarbons [7]. When LNG is released from containment onto land or water, it forms a pool that generates a visible LNG vapor cloud. As LNG evaporates, the methane vaporizes faster than the heavier components due to its lower boiling point. As a result, vapor will be preferentially methane rich, whereas the heavier components will stay in the liquid pool [3]. Therefore, the thermodynamic properties of methane can be used as a proxy to LNG vapor properties. When performing a dispersion simulation, the properties of a mixture corresponding to the composition of LNG must be specified as the fluid properties.

LNG vapor clouds are cold and contain aerosols which result from the condensation of the moisture in the air. Theoretically, the moisture imposes little effect

over the whole LNG dispersion process because of two opposite physical phenomena—condensation and evaporation occurring in turn. However, the latent heat from the phase change of moisture provides additional heat to warm up the LNG vapor at the onset, besides the sensible heat of the air, therefore relevant thermodynamic phenomena must be modeled to characterize their influence in dispersion calculations. Instead of introducing a sub-model especially for condensation and a complex heterogeneous system into the simulation, an alternative strategy to deal with this issue is to introduce a modified heat capacity for moist air (C_p') which takes into account both sensible heat and latent heat exchange. A similar approach is also used in FLACS by Gexcon [46]. Given the temperature and humidity, the modified heat capacity of moist air (C_p') can be calculated using Aspen Plus. Two calculation cases are shown in Fig. 31 Fig. 32: one is with the initial condition of T = 25 °C, RH =50 %; other is with the initial condition of T = 8 °C, RH = 55 %.

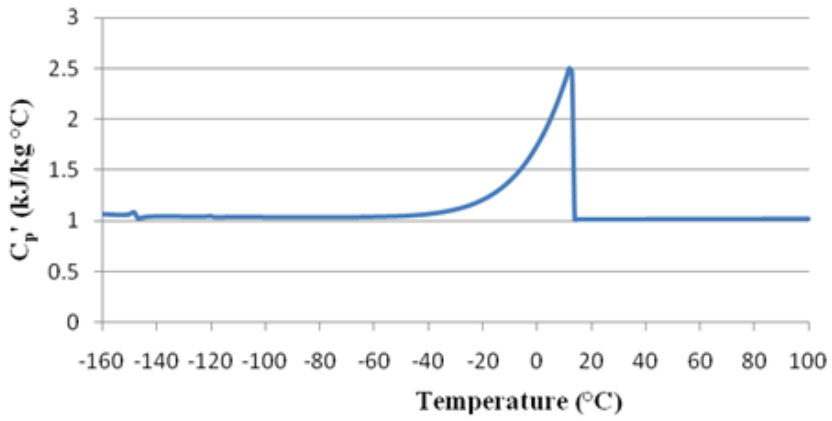

Fig. 31. Modified heat capacity of moist air with the initial condition of T=25°C, RH=50%

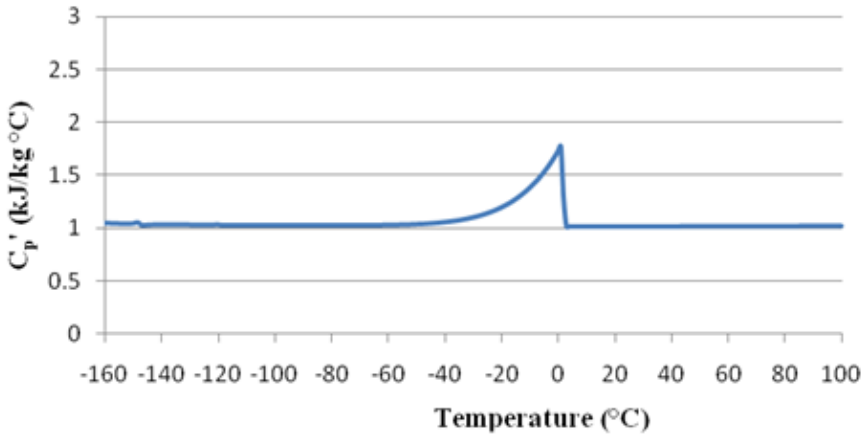

Fig. 32. Modified heat capacity of moist air with the initial condition of T=8°C, RH=55%

The dispersion of a vapor cloud in the atmosphere goes through three stages: negative buoyancy, neutral buoyancy, and positive buoyancy, depending on the temperature of the vapor cloud. At a temperature of 166 K, the density of methane is almost identical to that of air at a temperature of 289 K. Below 166 K, methane is negatively buoyant and more likely to accumulate in low areas. When the temperature is above 166 K, LNG vapor is positively buoyant and dissipates more easily in open areas, posing little flammable hazard to people and property on the ground [3]. If the release occurs in confinement, the buoyant vapor cloud is still hazardous as it might lead to a vapor cloud explosion. As the temperature increases, the LNG dispersion status changes from negative to positive buoyancy. Therefore, a buoyancy model is required to capture the density difference caused by the temperature variation. In ANSYS CFX, the full buoyancy model is recommended for simulating the buoyancy effect given that the fluid

density is a function of temperature. Within this model, the buoyancy reference density can be set to 1.225 kg/m^3 [47].

Similarly, a turbulence model must be identified to predict the effects of turbulence in the ambient atmosphere and LNG vapor. ANSYS CFX offers a large variety of turbulence models, such as the k-ε model, k-ω model, and shear stress transport (SST) model [48]. A comparative study of these turbulence models against experimental data has been reported elsewhere [55]. In the present work, the standard k-ε model was used because of its balance between computational time and precision. This model has been used for numerical simulations of LNG vapor dispersion and other dense gas dispersions with satisfactory results [44, 45, 56].

Finally, a heat transfer model is selected to represent the heat transfer throughout fluids within the domain. This model must take into account both the thermal energy and kinetic energy, which can be addressed in ANSYS CFX using the total energy model.

4.3.3.2 Atmosphere Boundary

The atmospheric surface layer is the region of interest where LNG vapor dispersion occurs following an accidental release. An accurate description of air flow in the atmospheric surface layer near the ground is of prime importance to make CFD codes generate reliable simulation results. Almost all atmosphere-related simulations have modeled the air flow in this layer as fully-developed horizontally homogeneous, in which the mean variables are only dependent on the height *z*. In a simulation with ANSYS CFX, the atmospheric boundary is always set as an open boundary, where fluids

can simultaneously flow in and out of the domain. Wind velocity, temperature, and turbulence profiles are developed to represent the characteristics of these variables in real situations. In the atmospheric surface layer, the momentum and heat vertical fluxes do not vary by more than 10%. Due to these small flux variations, the use of the Monin-Obukhov similarity theory is recommended to describe the wind velocity, temperature, and turbulence profiles [43, 57]. The wind velocity and potential temperature gradient functions along the height z are given as follows [22]:

$$\frac{\partial U}{\partial z} = \frac{U_*}{\kappa \cdot z} \cdot \phi_m \left(\frac{z}{L}\right) \tag{33}$$

$$\frac{\partial \theta}{\partial z} = \frac{\theta_*}{\kappa \cdot z} \cdot \phi_h \left(\frac{z}{L}\right) \tag{34}$$

where L, U_*, and θ_* are the Monin-Obukhov length, friction velocity, and scaling potential temperature, respectively, and κ is the von Karman constant (0.41).

Integrating the above equations from z_0 to z gives

$$U(z) = \frac{U_*}{\kappa}\left[\ln\left(\frac{z}{z_0}\right) - \psi_m \left(\frac{z}{L}\right)\right] \tag{35}$$

$$\theta(z) = \theta_0 + \frac{\theta_*}{\kappa}\left[\ln\left(\frac{z}{z_0}\right) - \psi_h \left(\frac{z}{L}\right)\right] \tag{36}$$

where

$$\psi_m \left(\frac{z}{L}\right) = \int_{z_0}^{z} \left(\frac{1}{z} - \frac{\phi_m \left(\frac{z}{L}\right)}{z}\right) dz \tag{37}$$

$$\psi_h\left(\frac{z}{L}\right) = \int_{z_0}^{z}\left(\frac{1}{z} - \frac{\phi_h\left(\frac{z}{L}\right)}{z}\right)dz \tag{38}$$

Here, z_0 is the surface roughness height and θ_0 is the potential temperature at z_0. The potential temperature is related to the ambient temperature and pressure by

$$\theta = T\left(\frac{P_0}{P}\right)^{\mu} \tag{39}$$

where T is the actual temperature, P is the actual pressure, P_0 is the standard reference pressure, and μ= 0.285. Generally, the potential and actual temperatures in the atmospheric surface layer, in absolute units, do not differ by more than 10% [58].

The Cartesian components of the wind velocity in three directions are then expressed by introducing the wind direction angle α,

$$U_x(z) = U(z) * cos(\alpha) \tag{40}$$

$$U_y(z) = U(z) * sin(\alpha) \tag{41}$$

$$U_z(z) = 0 \tag{42}$$

Air flow in the atmospheric surface layer is a type of external flow, which means the air flows over or across objects rather than through them. In such a case, ANSYS CFX cannot automatically calculate the turbulence characteristics, such as turbulence kinetic energy k and eddy dissipation rate ε. One approach to deal with this limitation is to relate these variables to the Monin-Obukhov length [59]:

$$k(z) = 5.48U_*^2\left[\frac{\phi_h\left(\frac{z}{L}\right)}{\phi_m\left(\frac{z}{L}\right)}\right]^{1/2} \tag{43}$$

$$\epsilon(z) = \frac{U_*^3}{\kappa \cdot z}\phi_h\left(\frac{z}{L}\right) \tag{44}$$

The functions $\phi_m\left(\frac{z}{L}\right), \phi_h\left(\frac{z}{L}\right), \psi_m\left(\frac{z}{L}\right), \psi_h\left(\frac{z}{L}\right)$ can be expressed as empirical relations with the Monin-Obukhov length [22]:

When $L>0$

$$\phi_m\left(\frac{z}{L}\right) = \phi_h\left(\frac{z}{L}\right) = 1 + 5\frac{z}{L} \tag{45}$$

$$\psi_m\left(\frac{z}{L}\right) = \psi_h\left(\frac{z}{L}\right) = -5\frac{z}{L} \tag{46}$$

When $L<0$

$$\phi_m\left(\frac{z}{L}\right) = \frac{1}{\mathrm{x}} \tag{47}$$

$$\phi_h\left(\frac{z}{L}\right) = \frac{1}{x^2} \tag{48}$$

$$\psi_m\left(\frac{z}{L}\right) = 2\ln\left[\frac{1+x}{2}\right] + \ln\left[\frac{1+x^2}{2}\right] - 2tan^{-1}(x) + \frac{\pi}{2} \tag{49}$$

$$\psi_h\left(\frac{z}{L}\right) = 2\ln\left[\frac{1+x^2}{2}\right] \tag{50}$$

with

$$x = \left(1 - \frac{16z}{L}\right)^{1/4} \tag{51}$$

To solve the above equations, the wind velocity and temperature must be measured at least at two different heights above the ground. Another alternative approach to represent the wind velocity and turbulence profiles associated with the k-ε

turbulence model if measurements are made at only one height is proposed as follows [60]:

$$U = \frac{U_*}{\kappa} \ln\left(\frac{z + z_0}{z_0}\right) \tag{52}$$

$$k = \frac{U_*^2}{\sqrt{C_\mu}} \tag{53}$$

$$\varepsilon = \frac{U_*^2}{\kappa(z + z_0)} \tag{54}$$

With this method, the temperature is assumed to be constant along the height *z*.

4.3.3.3 LNG Pool

The LNG pool can be specified as an inlet boundary, where the LNG vapor flows into the domain. The LNG pool area and shape, evaporation rate, vapor temperature, and turbulence in the source term are essential parameters required to describe the LNG pool boundary.

The pool area and shape depend on the surface properties and geometry of the spill area. When there is a release in an impoundment area, the LNG pool keeps the same area and shape as the impoundment due to the presence of boundaries. For an instantaneous release or continuous release of LNG in an open area, pool spreading models are required to determine the spread rate and area [24, 25, 61]. The commonly used model for calculating the free-spreading pool area in the case of continuous LNG release on water is [14]:

$$A_p = \frac{\dot{V}}{\dot{y}} \tag{55}$$

where $\dot{V}$ is the mean spill rate, A_p is the pool area, and $\dot{y}$ is the mean liquid regression rate,

$$\dot{y} = \frac{\dot{Q}}{\rho_L \lambda} \tag{56}$$

Here, $\dot{Q}$ is the mean heat flux to the pool, ρ_L is the liquid density, and λ is the liquid latent heat of vaporization.

The mean vapor velocity across the pool entering the domain can be determined by

$$v_g = \frac{\dot{m}_{liq}}{\rho_g \cdot A_p} \tag{57}$$

where v_g is the vapor velocity, $\dot{m}_{liq}$ is the LNG mass flow rate, and ρ_g is the LNG vapor density at the boiling point.

The recommended vapor temperature at this boundary is 111 K, which is the LNG boiling point under normal conditions.

The turbulence above the pool induced by vapor evaporation must be specified as part of the k-ε model requirements. The following equations provide the relationship between the turbulence kinetic energy and the energy dissipation rate with the turbulence intensity [43]:

$$k = \frac{3}{2}\left(v_g T_i\right)^2 \tag{58}$$

$$\varepsilon = C_\mu^{3/4} \frac{k^{3/2}}{0.07D} \tag{59}$$

where C_μ is the turbulence constant (0.09), T_i is the turbulence intensity and D is the LNG pool diameter.

4.3.3.4 Ground

The ground is set as a no-slip condition, which means the velocity on the surface is zero. Basic parameters that must be specified at the ground boundary include the heat flux or surface temperature. The heat flux from the ground to the atmosphere can be positive or negative, depending on the temperature difference between the ground and atmosphere.

Terrain and obstacles can be represented as geometrical features of the ground. The roughness of their surfaces in ANSYS CFX is expressed in terms of a roughness height or equivalent sand grain roughness, whose value is quite small. The determination of roughness height for different surface types is given by Wieringa [62]. Three different types of surface roughness should be distinguished in a CFD simulation: Z_0 is the overall surface roughness of the upstream out of the domain, which is obtained along with atmospheric profiles by solving Monin-Obukhov equations; Z_1 is the surface roughness of the ground in the domain, which keeps wind profile unchanged in the region free of obstacles; Z_2 is the surface roughness of explicitly modeled obstacles, whose value is often close to zero. These types of surface roughness are schematically shown in Fig. 33.

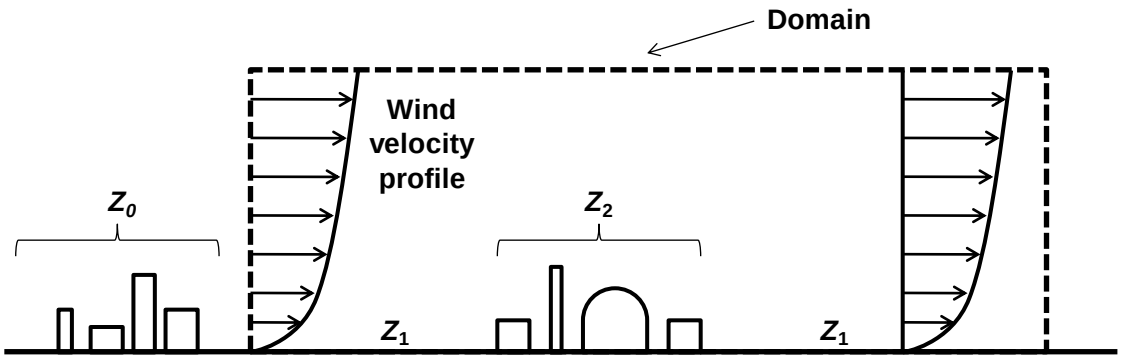

Fig. 33. Various surface roughness representation for CFD simulation

The wind velocity profile is one of the essential inputs at the inlet of the domain, which is always located far from major geometries. It is anticipated that wind velocity profile maintains unchanged unless encountering obstacles in the flow region. Achieving this anticipation is highly dependent on the proper selection of the value of Z_1. A sensitivity analysis with different Z_1 values ranging from 0 to 2 m is shown in Fig. 34 to illustrate the influence of Z_1 on the wind velocity profile.

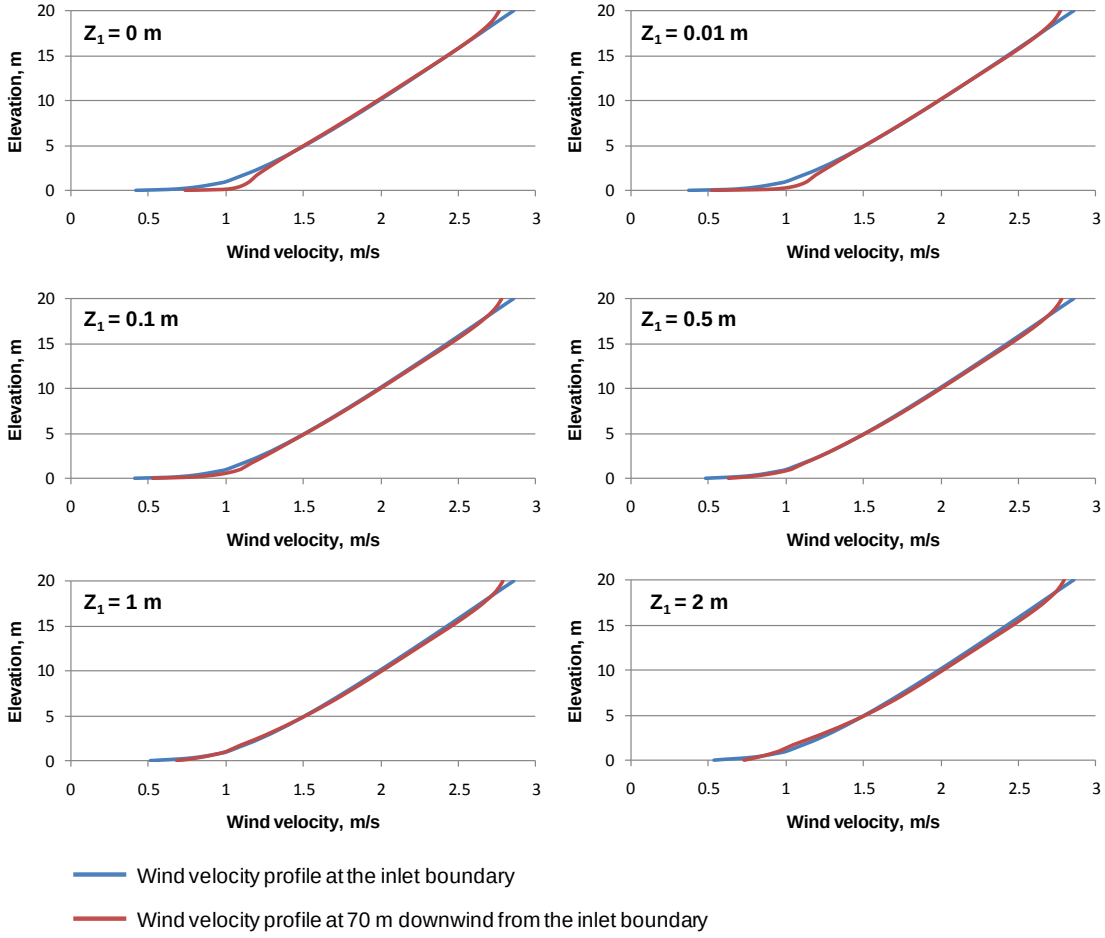

Fig. 34. Wind velocity profile change with different ground surface roughness height Z_1

4.3.3.5 Initial Conditions

The fluid mixture composition, height-dependent wind speed, ambient temperature, turbulence kinetic energy, and energy dissipation rate must be specified throughout the domain as initial conditions. These initial values were set close to values in the atmospheric boundary to create an initial state with only wind flow through the domain and no LNG vapor.

4.4 Simulation Specifications

The simulations were set up using the approach described in the previous section as well as input data from the MKOPSC LNG spill test database. For the simulation of Case I, data were exacted from the 2006 LNG vapor dispersion test database over a 45-s time interval, within which there was little variation in wind speed and direction, as shown in Table 9. Therefore, the data can better serve to study the underlying physical mechanism of LNG vapor dispersion and evaluate steady-state simulation results. For the simulation of Case II, transient simulations were conducted to compare downwind gas concentration profiles between test measurements and simulation results over the whole process of LNG release. The Case II input data are from the 2007 LNG vapor dispersion test, which are shown in Table 10.

Table 9. Summary of test data for Case I simulation

Parameter	Value
LNG flow rate, m^3/min	0.265
LNG pool diameter, m	4.6[a]
Average wind speed @ 3 m, m/s	1.8
Average wind speed @ 10 m, m/s	2.2
Average wind direction @ 3 m, degree	77[b]
Average wind direction @ 10 m, degree	94[b]
Temperature @ 3 m, K	299.65
Temperature @ 10 m, K	299.05
Absolute air pressure, Pa	99860
Relative humidity, %	64.5
Stability class	D
Monin-Obukhov length, m	498.3
Roughness height, m	0.01

[a] estimated from on-site observation

[b] 0 degree is true north

Table 10. Summary of test data for Case II simulation

Parameter	Value
LNG flow rate, m3/min	0.75
LNG pool diameter, m	6a
Average wind speed @ 2.3 m, m/s	1.2
Average wind speed @ 10 m, m/s	1.9
Average wind direction @ 2.3 m, degree	160b
Temperature @ 2.3 m, K	289.05
Temperature @ 10 m, K	289.05
Absolute air pressure, Pa	101300
Relative humidity, %	32.6
Stability class	B
Monin-Obukhov length, m	8.3
Roughness height, m	0.01

[a] estimated from temperature measurements on the water surface

[b] 0 degree is true north

Fig. 35 and 36 depict the geometric construction and meshing details of the test scenarios. The entire domain was mainly composed of tetrahedral cells, with a small amount of prism and pyramid cells in the inflation layers to better model the close-to-wall physics of the flow field such as the velocity gradient. Each simulation was solved

using convergence criteria based on a root mean square (RMS) residual of less than 1×10^{-4}. All simulation runs were carried out on a stand-alone desktop using an Intel Core2 Duo CPU E8500 with a clock speed of 3.16 GHz and 3.2 GB of RAM memory.

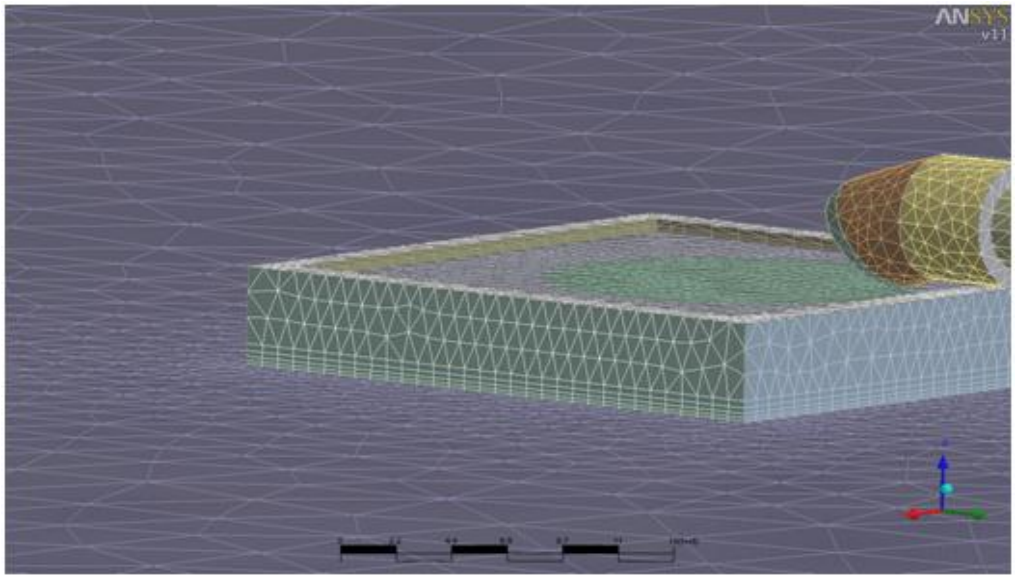

Fig. 35. Geometry construction and meshing details in Case I

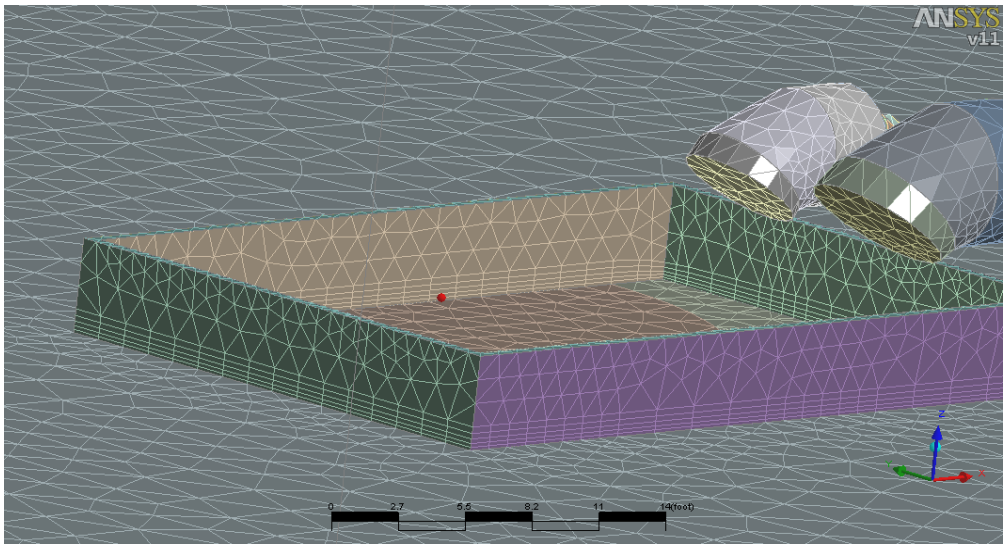

Fig. 36. Geometry construction and meshing details in Case II

4.5 Results and Discussion

4.5.1 Comparison between CFX Simulation Results and Test Data

Fig. 37 compares the plume shape of an on-site test photo and the simulation results in Case I. The photo was taken approximately 10 minutes after the start of the test. The visible boundary of the vapor plume corresponds to a vapor concentration of 3.5% v/v at a relative humidity of 64.5% [63], which can be represented by an isosurface of identical vapor concentration when post-possessing the simulation results. Fig. 37(a) shows a fog-like vapor cloud that formed as a result of the LNG release on water. The shape of the vapor plume gives an indication of the wind direction at that time. During the test, the vapor cloud wafted down from the edge of the pit and drifted near the ground as a dense gas for a certain distance. As the vapor cloud warmed up, it rose and diluted into the atmosphere. This physical process was reproduced in the CFX simulation, as shown in Fig. 37(b). In both figures, the plume above the pit was almost as high as the foam generator. After the vapor dispersed downward, its volume continued to become larger and larger. The overall height and width of the simulated plume was similar to the real one in source area and downwind. The physical behavior of the LNG vapor dispersion process in the test scenario was well characterized by the ANSYS CFX modeling, especially the vapor buoyancy variation from negative to positive. The effects of the geometry features (foam generator and pit) on the vapor cloud were also well represented.

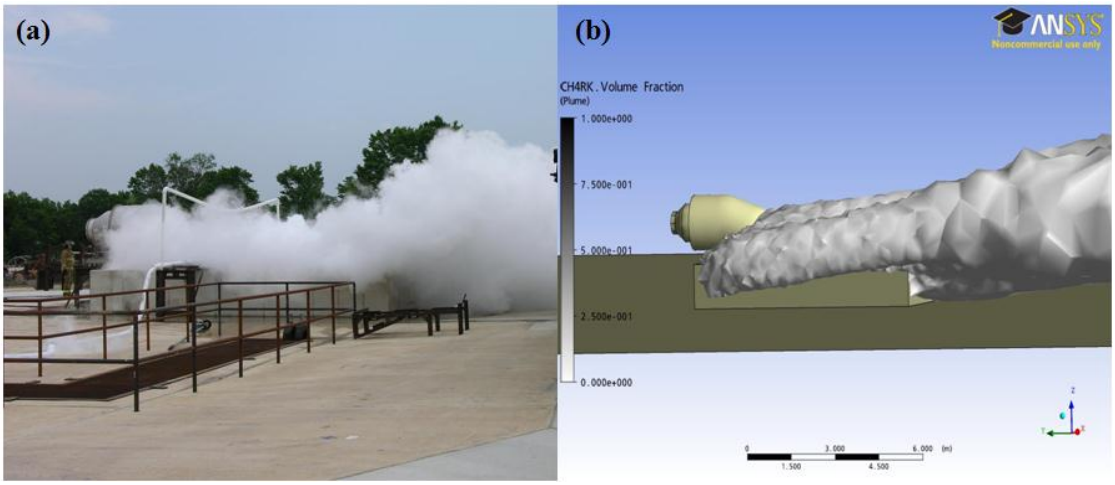

Fig. 37. Comparison of the plume shape of on-site photo and the simulation results. (a) On-site photo and (b) ANSYS CFX simulation

Fig. 38 and 39 show the LNG vapor temperature and air velocity profiles in the downwind vertical centerline plane. The temperature of the LNG vapor changed rapidly after the cold LNG vapor emanated from the pool. At this stage, it mixed with ambient air with intense heat transfer to form a vapor/air mixture. When the mixture drifted downwind, the majority of the heat and momentum transfer occurred at its boundary. As a result, the cloud's core was colder and more stable than its peripheral region. Due to the blockage of the foam generator in the upwind direction, there was a space under the foam generator with little wind and mild mixing with air. Because of this, the temperature of the vapor within this region changed more slowly than that of the vapor away from the foam generator. This indicates that the wind velocity and its turbulence have a strong influence on the temperature change of the vapor cloud and thus on the downwind distance to LFL.

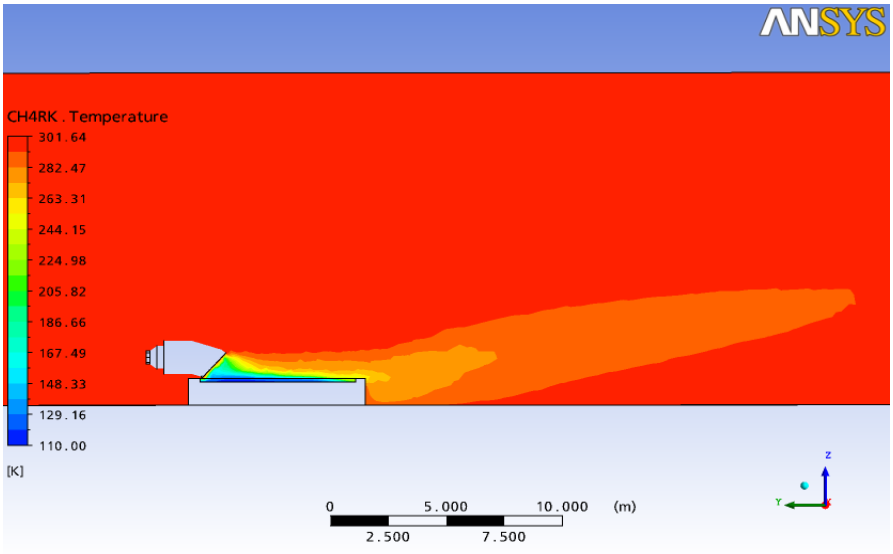

Fig. 38. Vapor temperature in the vertical centerline plane downwind

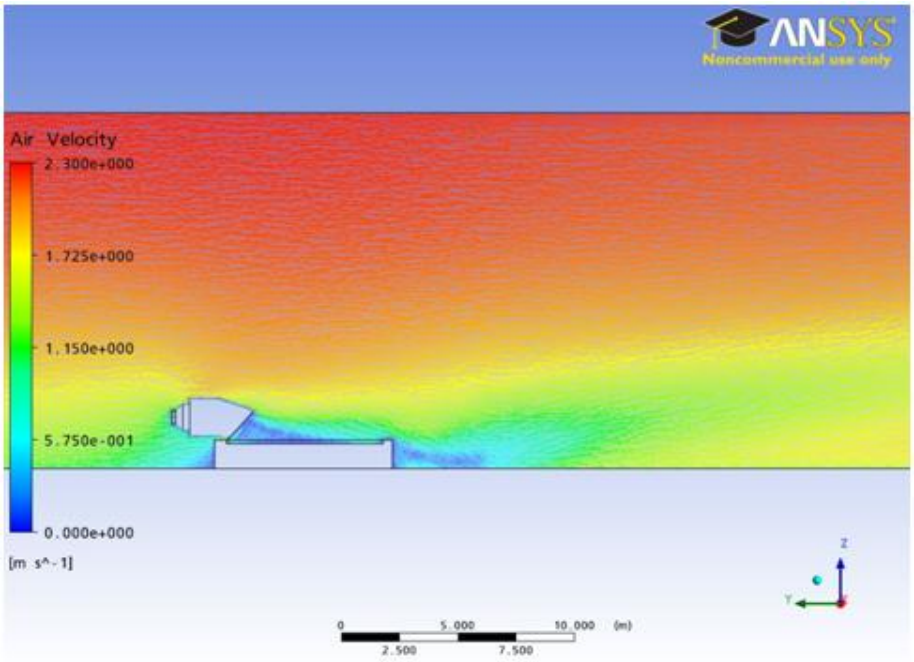

Fig. 39. Air velocity in the vertical centerline plane downwind

Fig. 40 compares the calculated methane volume fraction contours at 0.3 m elevation with contours generated by interpolating scattered experimental data using the Kriging method. It is evident that the simulation results are in reasonable overall agreement with test data within the rectangular area where gas detectors were installed to collect vapor concentration data in the test. Due to the effect of wind turbulence on the cloud, it is impossible to make simulated contours accurately match the actual ones. The measured ½ LFL distances at elevations of 0.3 and 1.22 m during the test ranged from 8.69–13.53 m and from 6.09–13.47 m respectively. Likewise, the simulation results show that the downwind distances to ½ LFL at these two elevations were about 9.8 m and 13.4 m, which were within the range of the test data.

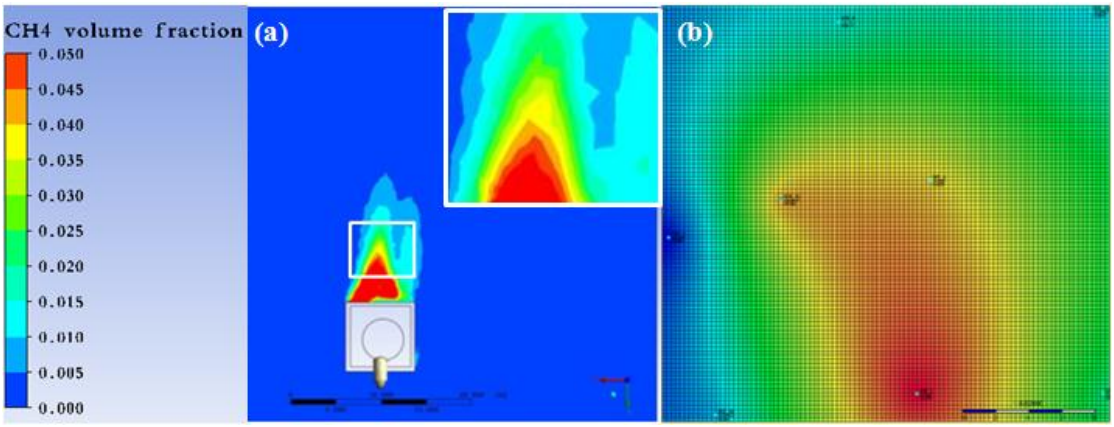

Fig. 40. Methane volume fraction contours at 0.3 m elevation downwind (Time = 600 s). (a) ANSYS CFX simulation and (b) Test data

Figs. 41 - 44 compare the predicted gas concentration profiles in Case II with test measurements at the same locations where gas detectors were installed. Fluctuations in

the on-site measurements resulted from the turbulence in the wind. It is noted that simulation results in Fig. 43 provide a reasonable overprediction of gas concentrations at 0.5 m elevation above the ground, which is desirable in exclusion zone determination. At 1.29 m elevation, the simulation results in Fig. 41, Fig. 42, and Fig. 44 fall into the range of concentration fluctuations and show underpredictions of concentration peak values. Moreover, higher gas concentrations appear close to the ground level in the simulation, as illustrated in Fig. 42 and 43, indicating the dense gas behavior of the LNG vapor cloud at the downwind distances where GDs 18 and 22 were located (same location but with different elevations). On the other hand, concentration readings from these two gas detectors reflect that vapors at the bottom have already become positive buoyant and promoted mixing inside the cloud. The over-assumption of dense gas behavior by the simulation therefore results in the underestimation of downwind gas concentrations at higher elevations above the ground, which might be attributed to the incomplete descriptions of heat transfer into the cloud in the simulation setup. The comparison of gas concentrations at two different heights illustrates that CFX is able to give reasonable overpredictions of flammable gas concentrations on the level close to the ground (below 0.5 m) but tends to underestimate concentrations at higher elevations. It overly assumes the slumping behavior of the LNG vapor cloud in the dispersion process and takes less into account buoyancy change from negative to positive as well as vapor mixing within the cloud.

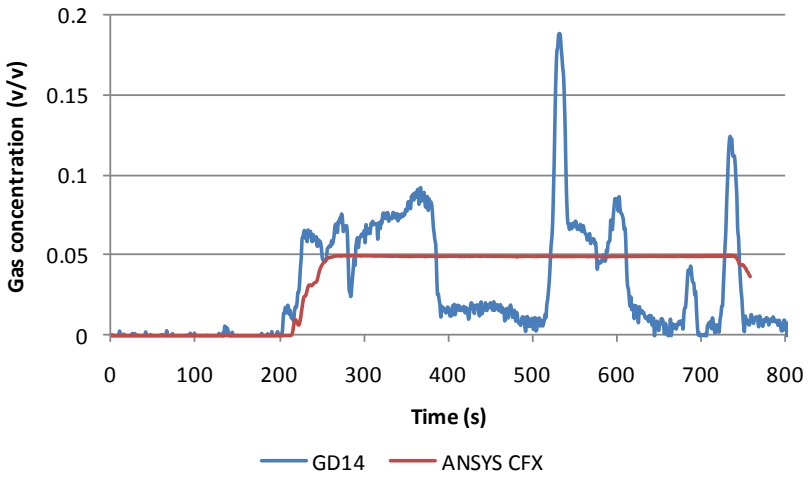

Fig. 41. Comparison of gas concentration in simulation result with test data from GD14 (x=4.9 m, y=-0.2 m, z= 1.29 m)

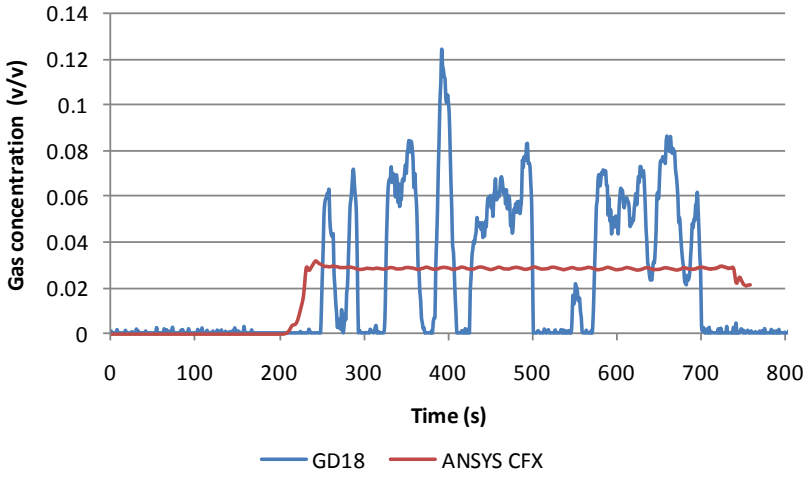

Fig. 42. Comparison of gas concentration in simulation result with test data from GD18 (x=-0.2 m, y=4.9 m, z= 1.29 m)

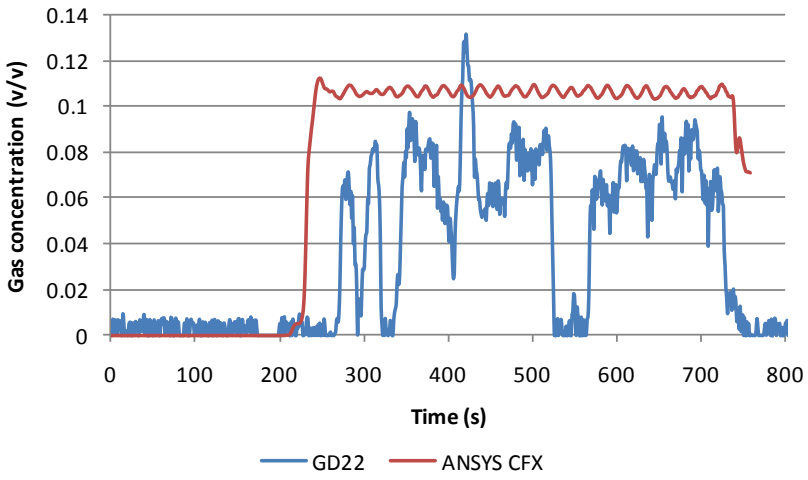

Fig. 43. Comparison of gas concentration in simulation result with test data from GD 22 (x=-0.2 m, y=4.9 m, z=0.5 m)

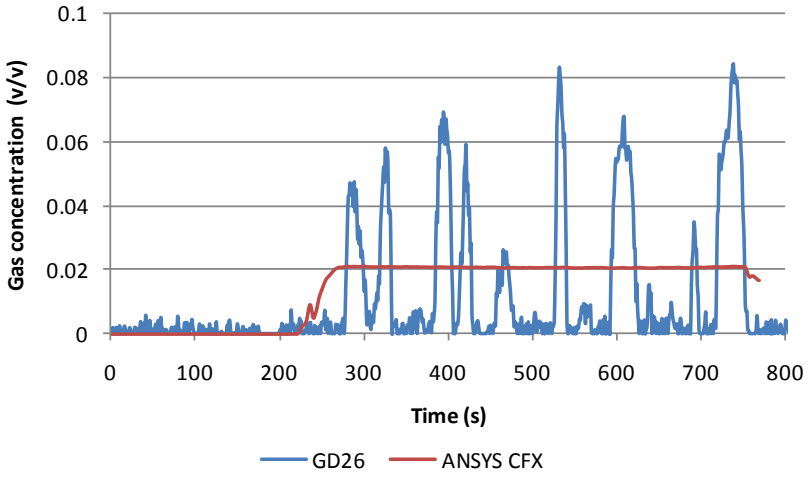

Fig. 44. Comparison of gas concentration in simulation result with test data from GD 26 (x=5.6 m, y=5.6 m, z= 1.29 m)

4.5.2 Uncertainty Sources in the CFX Simulation

Uncertainties in CFD simulation results arise from different sources, which can be generally categorized into two groups: 1) numerical errors and uncertainties and 2) errors and uncertainties in modeling the physics [64, 65]. The impact of sources in the two categories should be estimated and quantified through a sensitivity analysis in practical applications of CFD codes. If their influence on the accuracy of the simulation results cannot be ignored at certain confidence levels, further studies must be carried out on the methods to reduce or control the magnitude. Two examples are given below to illustrate the impact of two parameters, the mesh size and source term turbulence, on the simulation results.

4.5.2.1 Mesh Size Effect

Mesh size is a key parameter in controlling spatial discretization, which is associated with the truncation error of the Taylor series in the numerical method when calculating flow variable gradients at the face of a control volume. To evaluate the effect of the mesh size on the simulation results, a series of four runs was carried out with the same setup except for the size of the mesh. Table 11 shows the mesh information and simulation results for the ½ LFL, in which the maximum spacing was used in ANSYS CFX to set the maximum size of the mesh elements in the background of the domain.

Table 11. Mesh information and simulation results for Runs 1-4

	Run_1	Run_2	Run_3	Run_4
Maximum Spacing, m	3.66	2.74	1.83	0.91
Total number of nodes	22391	26256	51525	232687
Total number of tetrahedral	89536	104295	199326	1074757
Total number of pyramids	221	222	236	234
Total number of prisms	10076	11959	25870	72380
Total number of elements	99833	116476	225432	1147371
Total running time, min	11.75	11.9	112.17	92.66
½ LFL at 0.3 m elevation, m	7.7	7.6	10	9.8
½ LFL at 1.22 m elevation, m	17.5	18.3	18.6	13.4

The total running time is determined by the number of iterations and the running time for each iteration, the latter of which is related to the total number of meshing elements. As shown in Table 11, Run_4 had almost five times the number of elements compared to Run_3; therefore it took more time for each iteration. However, Run_3 went through 457 iterations to achieve final convergence while Run_4 only used 82 iterations to obtain the same convergence because of the mesh quality improvement by decreasing mesh size. As a result, the total running time for Run_3 was longer than Run_4.

Fig. 46 shows contours of the vapor fraction in a downwind vertical centerline plane for Runs_1–4. Here, the 0.15 (UFL), 0.05 (LFL), and 0.025 (½ LFL) vapor volume fraction levels were of interest and were monitored to study the mesh size effect.

Due to insufficient number of meshing elements, the simulated vapor cloud did not depict a similar pattern as the cloud recorded in the experiment. A reliable numerical prediction could not be achieved with the default mesh size (Run_1). A finer mesh is required to reach desirable simulation accuracy. As shown in Fig. 46, when the mesh size was gradually decreased to 0.91 m (Run_4), the calculated ½ LFL at elevations of 0.3 and 1.22 m fell into the test data range.

In this study, a mesh-independent solution could not be achieved by repeating the calculations with successively refined meshes due to the limited available memory and computing power. For similar industrial cases, it is recommended to run simulations with two or three gradually decreasing mesh sizes and to compare the results to estimate the solution accuracy.

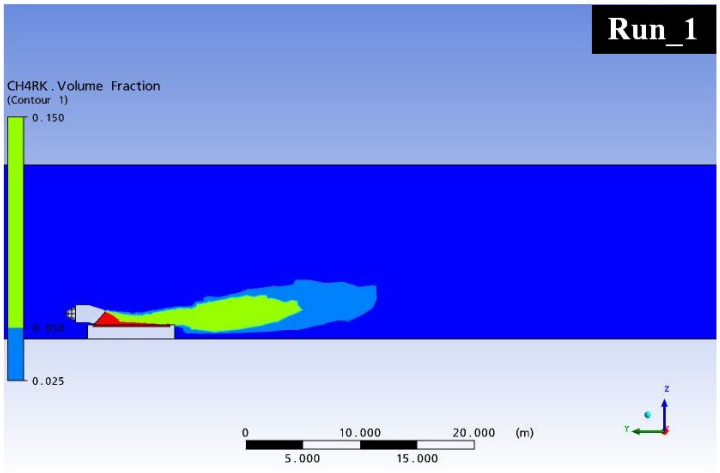

Fig. 45. Vapor fraction contours in the vertical centerline plane for Runs 1–4

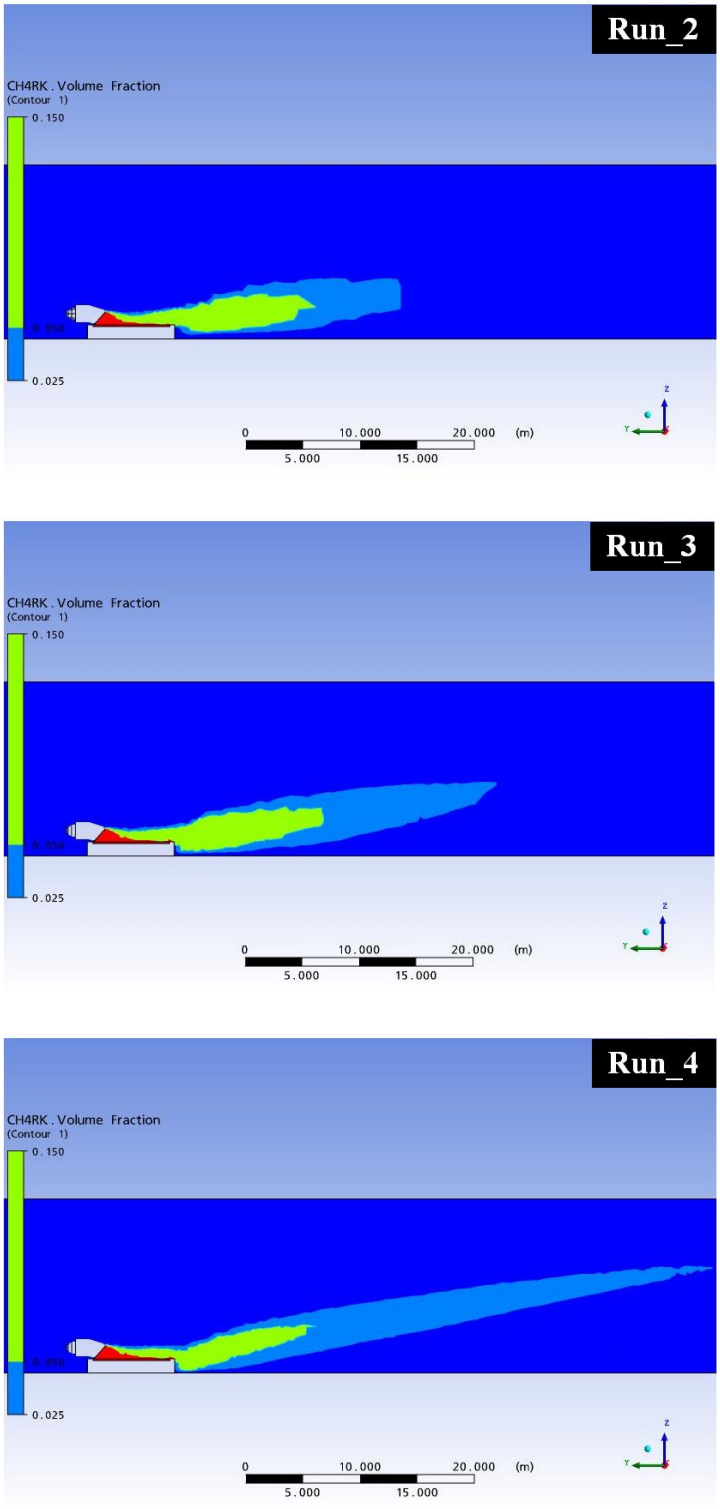

Fig. 46. Continued

4.5.2.2 Source Term Turbulence Intensity Effect

Another important parameter is the turbulence intensity in the source term which is associated with modeling vapor dispersion physical process. Turbulence intensity is the ratio of the standard deviation of the turbulent velocity fluctuations to the mean velocity. It characterizes the turbulence violence and determines the kinetic energy and energy dissipation rate above the poo. A series of four simulations were performed with different values of turbulence intensity in the source term to explore its influence on the simulation results. Table 12 shows the turbulence intensities and simulation results for the ½ LFL.

Table 12. Turbulence intensities and simulation results for Runs 5-8

	Run_5	Run_6	Run_7	Run_8
Turbulence intensity	1%	5%	10%	20%
½ LFL at 0.3 m elevation, m	0	0	11.2	9.8
½ LFL at 1.22 m elevation, m	4.1	13	11	13.4

Fig. 48 shows vapor fraction contours at an elevation of 1.22 m for Runs 5–8. In Run_5, where the level of turbulence is quite low, all volume fraction contours (UFL, LFL, and ½ LFL) almost overlapped. As the turbulent intensity gradually increased to 20% (Run_8), the predicted distance of the ½ LFL changed to almost three times the length of that given by Run_5. Thus, changing the turbulence intensity influences the shape of the vapor cloud and the prediction accuracy of the distance to flammable ranges.

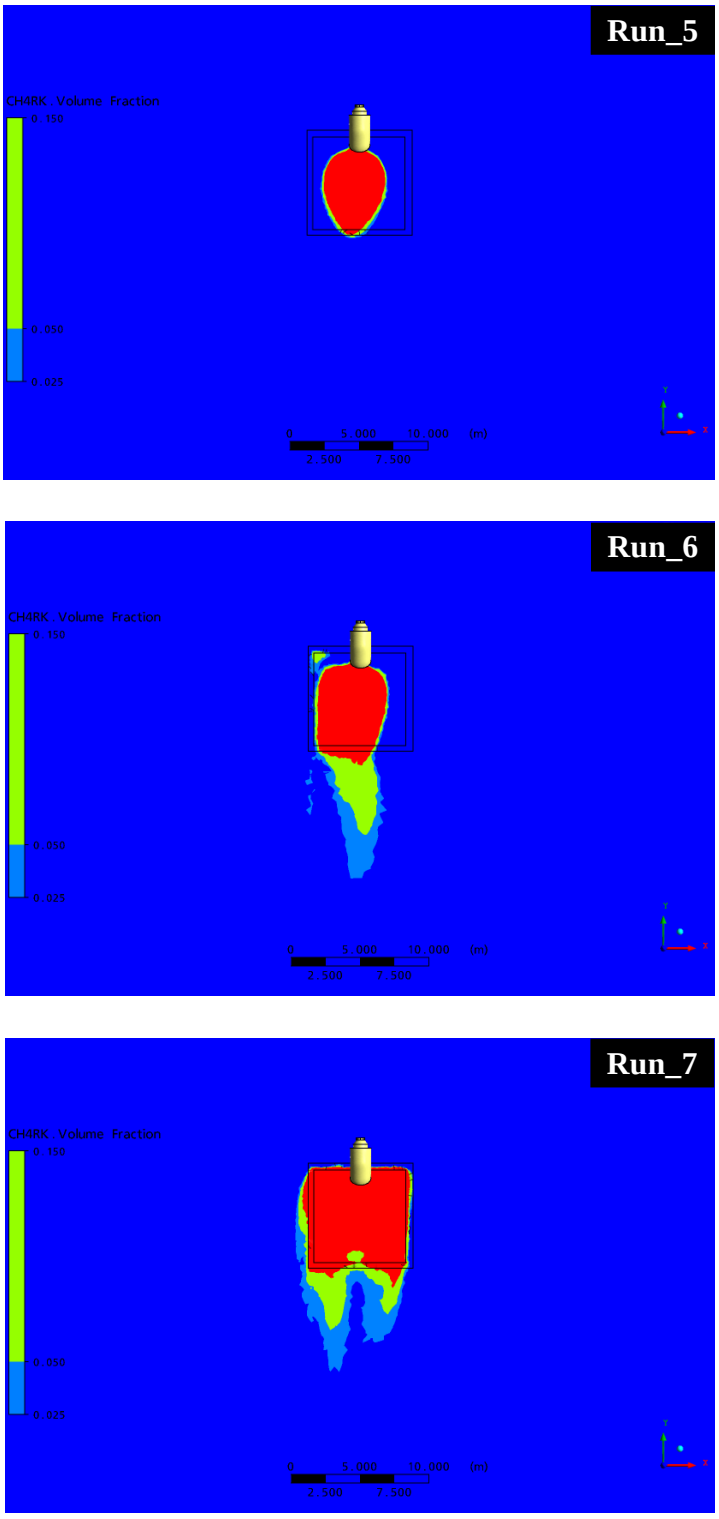

Fig. 47. Vapor fraction contours at an elevation of 1.22 m for Runs 5-8

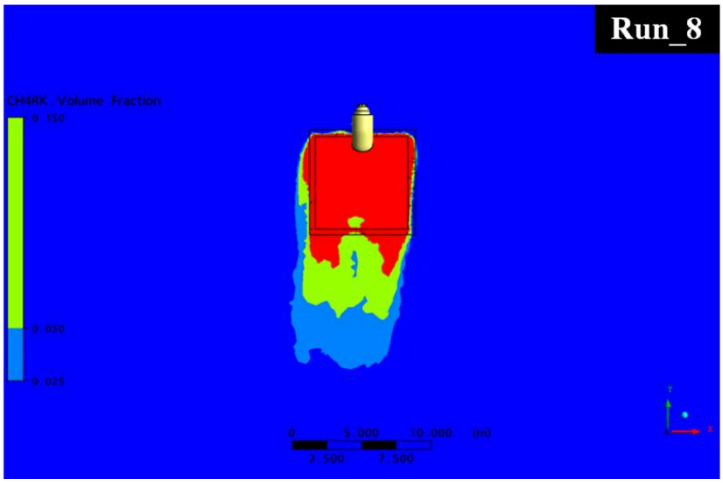

Fig. 48. Continued

4.6 Summary

This work uses the ANSYS CFX CFD code to model LNG vapor dispersion in the atmosphere. Discussed are important parameters that are essential inputs to the ANSYS CFX simulations, including the atmospheric conditions, humidity, LNG evaporation rate and pool area, turbulence in the source term, ground surface roughness height, and effects of obstacles. A sensitivity analysis was conducted to illustrate uncertainties in the simulation results arising from the mesh size and source term turbulence intensity. A comparison of test data with simulation results demonstrated that CFX was able to describe the dense gas behavior of LNG vapor cloud, and its prediction results of downwind gas concentrations close to ground level were in approximate agreement with the test data.

5. CONCLUSIONS AND RECOMMENDATIONS

5.1 Conclusions

Current source models are not capable of quantifying the potential hazards from LNG pipe leak underwater because of different physical behavior from an on-the-surface release of LNG. An underwater LNG release test was conducted to understand the phenomena that occur when LNG was released underwater and to determine the characteristic of the vapor emanating from the water surface. It was found that LNG release underwater in the form of a liquid jet resulted in very rapid breakup of the jet and the formation of vapor. The vapor formed was heated to a temperature higher than that corresponding to neutral buoyancy of vapor relative to air, even when the release depth was rather shallow (less than 1 m). It was also noted that LNG released underwater did not form a floating, boiling pool of LNG on the water surface. Instead, a buoyant vapor was released from the water surface. The formation of a visible, buoyant vapor depended upon the depth of release (the larger the depth the higher the vapor temperature at the water surface) and the water temperature. Besides, the general results from the test agreed with the predictions of a recently published theoretical model that simulated the phenomena that occur when LNG was released underwater.

ANSYS CFX was used to model LNG vapor dispersion modeling, and the simulation results were validated against medium-scale LNG spill tests at the BFTF. Essential parameters to setup a CFD simulation were identified and the influence of key parameters on simulation results was discussed. Some methods were introduced to

control or reduce the magnitude of uncertainties to a prescribed confidence level. Generally, CFX is able to effectively describe the dense gas behavior of LNG vapor dispersion in the atmosphere, and with appropriate setup inputs its prediction results provide good approximation of safe separation distances on the level near the ground. Our simulated results also showed that CFX gave concentration underpredictions at higher elevations (e.g. at 1.29 m elevation) because of the over-assumption of dense gas behavior of LNG cloud in the simulation. It is believed that complete representations of heat transfer from various sources to the LNG vapor cloud could contribute to the improvement of the reliability of CFX prediction results. Moreover, some numerical or physical parameters, such as mesh size and source term turbulent intensity, have a significant impact on the simulation accuracy. A sensitivity analysis was recommended to estimate and reduce the magnitude of errors related to numerical solution methods. To obtain the best possible prediction results out of CFX with available computing resources, more experimental work is needed to study the parameters that are essential to characterize the physical process of LNG vapor dispersion.

5.2 Recommendations for Further Research

5.2.1 Source Term Study

The experimental results from the LNG underwater release have a profound impact on predicted hazard distances arising from LNG releases from ships on to the water surface. In view of the results indicated in Section 3, the currently used scenarios of vapor dispersion and pool fire radiant heat and the calculations of the hazard distances

for spills from LNG carriers may not correctly signify the hazard scenarios or the distances to hazards.

When LNG is released from a height above the water surface (as from a hole, above the water line, in the hull and tank of a LNG carrier), it is expected to form a liquid jet that falls onto the water surface with a significant velocity. This jet will penetrate the water surface to depth that is measureable in meters. It is conceivable, based on the observations from the LNG underwater release test, that the LNG jet penetrating into the water will shatter and produce small droplets of LNG. Because of the expected high heat transfer rates between water and the LNG droplets, rapid evaporation will occur followed by water heating of the rising vapor so that when the vapor emanates from the water surface it is buoyant.

Since the test has shown that even at shallow release depths the vapor emanating at the water surface is buoyant and no LNG pool occurred on the water surface, it can be safely postulated that all or a significant part of the LNG jet from a tanker penetrating into water will evaporate and produce either no LNG pool on the water surface or a very small diameter pool (compared to current predictions). The vapor generated and released at the water surface will be positively buoyant and disperse as a normal temperature natural gas.

The upshot of the above discussion on the LNG jet-into-water phenomenon is that in the unlikely event of a LNG pool formation on the water surface it would be of small diameter and if this pool sustains a pool fire its radiant heat effects will be felt at much smaller distances than has been predicted in the current models. There will be no

heavy-gas dispersion hazard since the vapor will disperse buoyantly as an ambient temperature natural gas. Finally, if the gas being released is ignited, it would most likely burn in the form of set of fireballs released at intervals of several seconds (time dependent on the rate of gas release and the area of release at the water surface). This latter type of fire hazard has not been addressed in any of the off-shore LNG facility EIS.

It is necessary to conduct additional scaled tests to study the above phenomena in more detail. The previous underwater release test was of a very modest size and the instrumentation was not originally designed with a view to conducting an underwater LNG release test. No controlled tests have been performed with LNG release in the form of a turbulent jet plunging into a water body. Also, additional underwater LNG release tests with a greater range of variation in several important parameters (such as the depth, orientation of release, release rate and water temperature) need to be undertaken before definitive models can be developed to assess hazards.

5.2.2 Passive Mitigation System Study Using CFD Model

In the case of an accidental release, LNG will be guided to an impoundment where LNG can be controlled. In many LNG installations, concrete trenches are used to guide the LNG. There is no study on the effect that trench will impose on vapor dispersion. NFPA 59A or 49 CFR 193 does not address the design and mitigation system associated with trench, therefore there are no details on how it should be ideally designed.

The vapor holdup has to be determined to estimate the buoyancy of the cloud once it reaches out of the trench. CFD modeling could be used to understand the two-phase flow pattern (i.e., cryogenic LNG liquid with evaporated vapor), and estimate the vapor holdup, gradients of temperature, pressure, density and composition or LFL along the trench so that the trench design (e.g., shape, size and length of trench connecting the release source to the impoundment sump) can be optimized with more inherent safety.

In addition, passive barriers could be studied using CFD modeling in order to make the vapor positively buoyant before it reaches the wind entrainment. Since no experimental data are available to address these concerns, field experiments with simulated scenarios would be beneficial to understand the physical process and validate CFD modeling results.

REFERENCES

[1] M. Hightower, L. Gritzo, A. Luketa-Hanlin, J. Covan, S. Tieszen, G. Wellman, M. Irwin, M. Kaneshige, B. Melof, C. Morrow, D. Ragland, Guidance on Risk Analysis and Safety Implications of a Large Liquefied Natural Gas (LNG) Spill Over Water, SAND2004-6258, Sandia National Laboratories, Albuquerque, NM, 2004.

[2] V.L. Thorndike, LNG: A Level-Headed Look at the Liquefied Natural Gas Controversy, Versa Press, East Peoria, IL, 2007.

[3] Institution of Chemical Engineers (IChemE), BP Process Safety Series-LNG Fire Protection & Emergency Response, IChemE, UK, 2007.

[4] Mary Kay O'Connor Process Safety Center (MKOPSC), White Paper: LNG Pool Fire Modeling, M.S. Mannan (Editor), MKOPSC, Texas A&M University, College Station, TX 77843- 3122, September 2008.

[5] U.S. Energy Information Administration (EIA), Annual Energy Outlook 2010 with Projections to 2035, DOE/EIA-0383, 2010.

[6] Center for Liquefied Natural Gas, available from http://www.lngfacts.org/About-LNG/Filling-Supply-Demand-Gap.asp.[accessed on January 10 2011]

[7] M.M. Foss, Introduction to LNG: An overview on liquefied natural gas (LNG), it properties, organization of the LNG industry and safety considerations, Center for Energy Economics, University of Texas at Austin, Houston, TX, 2007.

[8] BP, BP Statistical Review of World Energy, June 2010, available from www.bp.com/statisticalreview.

[9] X. Wang, M. Economides, Advanced Natural Gas Engineering, Gulf Publishing Company, 2009.

[10] M. Barclay, Natural gas liquefaction process selection for emerging markets, Paper presented at 5th Doha Conference on Natural Gas, Doha, Qatar, March 2, 2005.

[11] U.S. Bureau of Mines, Report on the Investigation of the Fire at the Liquefaction, Storage, and Regasification Plant of the East Ohio Gas Co., Cleveland, Ohio, February 1946.

[12] CH-IV International, Safety History of International LNG Operations, March 2009.

[13] U.S. Government Accountability Office (GAO), Maritime Security: Public Safety Consequences of a Terrorist Attack on a Tanker Carrying Liquefied Natural Gas Need Clarification, GAO, February 2007

[14] B.R. Cormier, J. Suardin, M. Rana, Y. Zhang, Development of design and safety specifications for LNG facilities based on experimental and theoretical research, in: E.R. Pitt, C.N. Leung (Eds.), OPEC, Oil Prices and LNG, Nova Science Publishers, 2009.

[15] C.D. Zinn, LNG codes and process safety, Process Saf. Prog. 24 (2005) 158-167.

[16] J.A. Alderman, Introduction to LNG safety, Process Saf. Prog. 24 (2005) 144-151.

[17] Y. Qiao, H.H. West, M.S. Mannan, D.W. Johnson, J.B. Cornwell, Assessment of the effects of release variables on the consequences of LNG spillage onto water using FERC models, J. Hazard. Mater. 130 (2006) 155-162.

[18] R.P. Koopman, R.T. Cederwall, D.L. Ermak, H.C. Goldwire, Jr., W.J. Hogan, et al., Analysis of Burro series 40 m^3 LNG spill experiments, J. Hazard. Mater. 6 (1982) 43–83.

[19] R.P. Koopman, R.T. Cederwall, D.L. Ermak, H.C. Goldwire, Jr., W.J. Hogan,et al., Burro Series Data Report LLNL/NWC 1980 LNG Spill Tests, UCID-19075, Lawrence Livermore National Laboratory, 1982.

[20] J.S. Puttock, D.R. Blackmore, G.W. Colenbrander, Field experiments on dense gas dispersion, J. Hazard. Mater. 6 (1982) 13–41.

[21] H.C. Rodean,W.J. Hogan, P.A. Urtiew, H.C. Goldwire, Jr., T.G. McRae, et al., Vapor Burn Analysis for the Coyote Series LNG Spill Experiments, UCRL-53530, Lawrence Livermore National Laboratory, 1984.

[22] T.C. Brown, R.T. Cederwall, S.T. Chan, D.L. Ermak, R.P. Koopman, K.C. Lamson, J.W. McClure, L.K. Morris, Falcon Series Data Report: 1987 LNG Vapor Barrier Verification Field Trials, Lawrence Livermore National Laboratory, UCRL-CR-104316, June 1990.

[23] D.A. Crowl, J.F. Louvar, Chemical Process Safety: Fundamentals with Applications, 2nd ed., Prentice Hall PTR, NJ, 2002.

[24] J.A. Fay, Model of spills and fires from LNG and oil tankers, J. Hazard. Mater. 96 (2003) 171-188.

[25] F. Briscoe, P. Shaw, Spread and evaporation of liquid, Prog. Energy Comb. Sci. 6 (1980) 127–140.

[26] G.A. Melhem, LNG Release Assessment, Arthur D. Little, Cambridge, MA, 1991

[27] T.O. Spicer, J.A. Havens, Field test validation of the degadis model, J. Hazard. Mater. 16 (1987) 231-245.

[28] D.L. Ermak, S.T. Chan, D.L. Morgan, L.K. Morris, A comparison of dense gas dispersion model simulations with burro series LNG spill test results, J. Hazard. Mater. 6 (1982) 129-160.

[29] J.S. Puttock, Comparison of Thorney Island data with predictions of HEGABOX/HEGADAS, J. Hazard. Mater. 16 (1987) 439-455.

[30] R.K.S. Hankin, Heavy gas dispersion: Integral models and shallow layer models, J. Hazard. Mater. 102 (2003), 1–10.

[31] S.T. Chan, Numerical simulations of LNG vapor dispersion from a fenced storage area, J. Hazard. Mater. 30 (1992) 195-224.

[32] S.T. Chan, FEM3C: An improved three-dimensional heavy-gas dispersion model: User's manual, UCRL-MA-116567, Lawrence Livermore National Laboratory, December 1994.

[33] M.A. Rana, Forced Dispersion of Liquefied Natural Gas Vapor Clouds with Water Spray Curtain Application, PhD dissertation at TAMU, College Station, TX, 2009.

[34] G.W. Yun, Control of Vapor Dispersion and Pool Fire of Liquefied Natural Gas (LNG) with Expansion Foam, PhD dissertation at TAMU, College Station, TX, 2010.

[35] Mary Kay O'Connor Process Safety Center (MKOPSC), Data Report of MKOPSC LNG Spill Tests: 2005 -2009, MKOPSC, Texas A&M University, College Station, TX, 2010.

[36] J.D. Weise, Letter from Weise, Associate Administrator for Pipeline Safety, Pipeline and Hazardous Materials Administration, U.S. Department of Transportation to J.C. Wright, Director, Office of Energy Projects, Federal Energy Regulatory Commission, Washington, DC, July 2009.

[37] P.K. Raj, L.A. Bowdoin, Underwater LNG Release: Does a pool form on the water surface? What are the characteristics of the vapor released? J. Loss. Prev. Process Ind. 23 (2010) 753-761.

[38] D.S. Burgess, J.N. Murphy, M.G. Zabetakis, Hazards of LNG Spillage into Water, Final report to US Coast Guard, PMSRC Report No. S-4177, US Bureau of Mines, Dept. of the Interior, Pittsburgh, PA , September 1972

[39] D.R. Blackmore, G.W. Colenbrander, J.S. Puttock, Maplin Sands Experiments 1980: Dispersion results from continuous releases of refrigerated liquid propane and LNG, NATO, Challenges of Modern Society - Air Pollution Modelling and its Application, v 5, (editor, C.Wispelaere), Plenum, New York, pp. 353-373, 1984

[40] Title 49 Code of Federal Regulations Part 193(49-CFR-193): Liquefied Natural Gas Facilities: Federal Safety Standards, U.S. Government Printing Office, Washington, DC, 1980.

[41] National Fire Protection Association (NFPA), NFPA 59A: Standard for the Production, Storage, and Handling of Liquefied Natural Gas (LNG), NFPA, Quincy, MA, 2009.

[42] A. Luketa-Hanlin, A review of large-scale LNG spills: Experiments and modeling, J. Hazard. Mater.132 (2006) 119-140.

[43] A. Luketa-Hanlin, R.P. Koopman, D.L. Ermak, On the application of computational fluid dynamics codes for liquefied natural gas dispersion, J. Hazard. Mater. 140 (2007) 504-517.

[44] F. Gavelli, E. Bullister, H. Kytomaa, Application of CFD (Fluent) to LNG spills into geometrically complex environments, J. Hazard. Mater.159 (2008) 158-168.

[45] S. Sklavounos, F. Rigas, Simulation of Coyote series trials--Part I: CFD estimation of non-isothermal LNG releases and comparison with box-model predictions, Chem. Eng. Sci. 61 (2006) 1434-1443

[46] O.R. Hansen, J.A. Melheim, I.E. Storvik, CFD modeling of LNG dispersion experiments, AIChE Spring National Meeting, Houston, TX, 2007.

[47] B.R. Cormier, R. Qi, G. Yun, Y. Zhang, M.S. Mannan, Application of computational fluid dynamics for LNG vapor dispersion modeling: A study of key parameters, J. Loss. Prev. Process Ind. 22 (2009) 332-352.

[48] ANSYS CFX-Solver Theory Guide, ANSYS Ltd., 2006.

[49] N. Ashgriz, J. Mostaghimi, An introduction to computational fluid dynamics, in: J. Saleh, Fluid Flow Handbook, McGraw-Hill Professional, 2002, pp. 24.1-24.52.

[50] M.J. Ivings, S.F. Jagger, C.J. Lea, D.M. Webber, Evaluating Vapor Dispersion Models for Safety Analysis of LNG Facilities, Health & Safety Laboratory, UK, 2007.

[51] ANSYS CFX-Post User's Guide, ANSYS Ltd., 2006.

[52] H.K. Versteeg and W. Malalasekera, An Introduction to Computational Fluid Dynamics: The Finite Volume Method, second ed., Prentice Hall, 2007.

[53] H.A. Olvera, A.R. Choudhuri, Numerical simulation of hydrogen dispersion in the vicinity of a cubical building in stable stratified atmospheres, Int. J. Hydrogen Energy 31 (2006) 2356-2369.

[54] Release 11.0 Documentation for ANSYS Workbench, ANSYS Ltd., 2006.

[55] S. Sklavounos, F. Rigas, Validation of turbulence models in heavy gas dispersion over obstacles, J. Hazard. Mater. 108 (2004) 9-20.

[56] G.A. Perdikaris and F. Mayinger, Numerical simulation of heavy gas cloud dispersion within topographically complex terrain, J. Loss. Prev. Process Ind. 7 (1994) 391-396.

[57] B. Blocken, T. Stathopoulos, J. Carmeliet, CFD simulation of the atmospheric boundary layer: Wall function problems, Atmos. Environ. 41 (2007) 238-252.

[58] S.P. Arya, Introduction to Micrometeorology, second ed., Academic Press, San Diego, CA, 2001.

[59] H.A. Panofsky, J.A. Dutton, Atmospheric Turbulence: Models and Methods for Engineering Applications, Wiley, NY, 1984.

[60] P.J Richards, R.P Hoxey, Appropriate boundary conditions for computational wind engineering models using the k–ε turbulence model, J. Wind Eng. Ind. Aero. 46-47 (1993) 145-153.

[61] D.W. Hissong, Keys to modeling LNG spills on water, J. Hazard. Mater. 140 (2007) 465-477.

[62] J. Wieringa, Updating the Davenport roughness classification, J. Wind Eng. Ind. Aero. 41 (1992) 357-368.

[63] P.K. Raj, Where in a LNG vapor cloud is the flammable concentration relative to the visible cloud boundary, NFPA Journal, May/Jun 2006.

[64] H.W. Coleman, F. Stern, Uncertainties and CFD code validation, J. Fluids Eng. 119 (1997) 795-803.

[65] J. Tu, G. H. Yeoh, C. Liu, Computational Fluid Dynamics-A Practical Approach, Butterworth-Heinemann, Oxford, UK, 2008.

VITA

Ruifeng Qi was born in Fushun, Liaoning, China. He received his Bachelor of Engineering degree in chemical engineering and technology from Dalian University of Technology in July 2006. He entered the graduate program in chemical engineering at Texas A&M University, College Station, Texas in August 2006 and received his Doctor of Philosophy degree in August 2011. His research interests include LNG field experiments and consequence modeling.

Mr. Qi may be reached at the Mary Kay O'Connor Process Safety Center, Jack E. Brown Building, Texas A&M University, TAMU 3122, College Station, TX 77843. His email is qiruifeng@gmail.com.